HHS Public Access

Author manuscript

Biophys Chem. Author manuscript; available in PMC 2024 October 01.

Published in final edited form as:

Biophys Chem. 2024 September ; 312: 107285. doi:10.1016/j.bpc.2024.107285.

Understanding the Structural Dynamics of Human Islet Amyloid Polypeptide: Advancements in and Applications of Ion-Mobility Mass Spectrometry

Zijie Dai[1], **Aisha Ben-Younis**[1], **Anna Vlachaki**[2], **Daniel Raleigh**[1,3,*], **Konstantinos Thalassinos**[1,4,*]

[1]Institute of Structural and Molecular Biology, Division of Bioscience, University College London, London, WC1E 6BT, U.K.

[2]Department of Clinical Neurosciences, John van Geest Centre for Brain Repair, University of Cambridge, Forvie Site, Robinson Way, Cambridge, CB2 0PY, UK

[3]Department of Chemistry, Stony Brook University, 100 Nicolls Road, Stony Brook, New York 11794, United States.

[4]Institute of Structural and Molecular Biology, Birkbeck College, University of London, London WC1E 7HX, U.K.

Abstract

Human islet amyloid polypeptide (hIAPP) forms amyloid deposits that contribute to β-cell death in pancreatic islets and are considered a hallmark of Type II diabetes Mellitus (T2DM). Evidence suggests that the early oligomers of hIAPP formed during the aggregation process are the primary pathological agent in islet amyloid induced β-cell death. The self-assembly mechanism of hIAPP, however, remains elusive, largely due to limitations in conventional biophysical techniques for probing the distribution or capturing detailed structures of the early, structurally dynamic oligomers. The advent of Ion-mobility Mass Spectrometry (IM-MS) has enabled the characterisation of hIAPP early oligomers in the gas phase, paving the way towards a deeper understanding of the oligomerisation mechanism and the correlation of structural information with the cytotoxicity of the oligomers. The sensitivity and the rapid structural characterisation provided by IM-MS also show promise in screening hIAPP inhibitors, categorising their modes of inhibition through “spectral fingerprints”. This review delves into the application of IM-MS to the dissection of the complex steps of hIAPP oligomerisation, examining the inhibitory influence of metal ions, and exploring the characterisation of hetero-oligomerisation with different hIAPP variants. We highlight the potential of IM-MS as a tool for the high-throughput screening of hIAPP inhibitors, and for providing insights into their modes of action. Finally, we discuss advances afforded by recent advancements in tandem IM-MS and the combination of gas phase spectroscopy with IM-MS, which promise to deliver a more sensitive and higher-resolution structural portrait of hIAPP oligomers. Such information may help facilitate a new era of targeted therapeutic strategies for islet amyloidosis in T2DM.

*Corresponding authors: d.raleigh@ucl.ac.uk, k.thalassinos@ucl.ac.uk.

Graphical Abstract

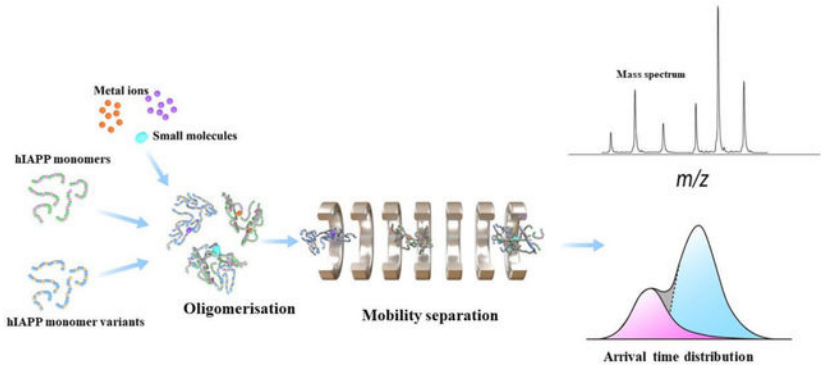

Keywords

Amylin; IAPP; Ion-mobility mass spectrometry; Mass spectrometry; Protein aggregation; Type-II diabetes Mellitus

1. Introduction

1.1 Islet Amyloid polypeptide

Islet amyloid polypeptide (IAPP, also known as amylin) is a 37-residue polypeptide hormone synthesised in the pancreatic insulin-producing β-cells. IAPP was originally isolated from amyloid deposits in the pancreatic islets of Langerhans from patients who had type-2 diabetes (T2D). IAPP is co-stored with insulin from the secretory granules in pancreatic β-cells in the islets of Langerhans and is released in response to the same stimuli that lead to insulin secretion (1–3). hIAPP has been shown to have essential roles in regulating metabolism and glucose homeostasis, by inhibiting postprandial glucagon release from α-cells (4). Additionally, IAPP influences gastric emptying and satiety (4, 5). It also traverses the blood-brain barrier (BBB), influencing the release of pancreatic hormones and the control of appetite (6).

Human islet amyloid polypeptide (hIAPP), however, forms pancreatic islet amyloid in T2D and in the pre-diabetic state. The process of amyloid formation contributes to β-cell death and dysfunction, exacerbating the disease and often compromising the success of islet transplantation (7, 8). The mechanisms of hIAPP amyloid formation, both *in vivo* and *in vitro*, are poorly understood.

hIAPP is synthesised as an 89-residue Prepro-IAPP, derived from the expression of the *IAPP* gene. Prepro-IAPP is first processed by cleavage of its 22-residue signal peptide to yield a 67-residue Pro-IAPP polypeptide (9). Subsequent cleavage of Pro-IAPP and post-translational modifications (PTMs) occurs within the Golgi apparatus and the insulin β-cell secretory granules, culminating in the production of the 37-residue mature hIAPP (Fig.1). Mature hIAPP has an amidated C-terminus and a disulphide bridge between residues Cys2 and Cys7 (10–13). The processing is vital as the C-terminus is required for full biological

activity (14), and several studies have suggested that aberrations in this sequence may lead to increased formation of islet amyloids (13, 15).

Native human IAPP (hIAPP) is categorized as an intrinsically disordered protein, which lacks a defined and stable globular structure but instead transiently adopts various rapidly converting and partially structured alpha-helical conformations (16, 17). hIAPP and its dimer form, exhibit transiently adopted α-helical structure primarily at residues 8–18 (N-terminal region) and 22–27. The propensity of adopting such α-helical structure at the N-terminus has been proposed to be affected by the redox balance (18). The imbalance in the redox state may lead to ER stress, which has been proposed as one of the mechanisms of hIAPP-induced cytotoxicity in pancreatic β-cells (17, 18). The adoption of the partially structured α-helical conformation may facilitate the further conversion to β-conformation (17, 19, 20), which has a strong correlation with the early aggregation and cytotoxicity.

Comparison of IAPP from different species indicates that the amino acid sequences significantly influence amyloidogenicity and toxicity. Previous studies have shown that mice and rat IAPP (rIAPP) are non-amyloidogenic, whereas human IAPP readily aggregates into amyloid at neutral pH (21, 22). Notably, the region spanning residues 20–29 of hIAPP was initially considered as a critical ‘amyloidogenic core’ that might dictate IAPP amyloidogenicity. This was based on the observation that rat IAPP differs from the human peptide at six positions, five of which are located between residues 22 and 29 and three of which involve proline (23, 24). Studies of hIAPP variants with proline substitution outside the 20–29 region showed that they can abolish hIAPP amyloid formation (25, 26). Additionally, substitutions of Asn14 and Asn21 drastically affect amyloid fibril formation (25, 26). In contrast, substituting residues 18, 23 and 26 in rIAPP with the corresponding residues in hIAPP results in weak amyloidogenicity, even with the retention of the three proline residues (27). Thus, while these studies do not entirely diminish the importance of the 20–29 region in IAPP amyloidogenicity, they underscore the vital contributions of other regions on IAPP amyloid formation. Noh *et al.* recently conducted a sequence alignment of IAPP to generate consensus sequences (28). The study highlights distinctive characteristics of human IAPP, particularly the presence of residues His18, Phe23, and Ser29, alongside a notable absence of proline in the entire sequence (Fig.2). hIAPP contains a histidine at position 18, a residue occupied by arginine across all other primate sequences and prevalent in over 89% of the sequences examined. Proline substitutions in hIAPP have been observed to attenuate amyloid formation rates *in vitro* (23, 29), and the replacement at residue 28 has the most significant effect of the three prolines found in rat IAPP (30).

There are very few documented natural mutations of hIAPP. The Ser-20-Gly (S20G) missense mutation, predominantly found in individuals of Chinese and Japanese descent, has been associated with an increased risk of type-2 diabetes (31, 32). The S20G mutation, one of only two reported missense mutations in the IAPP gene, accelerates amyloid formation *in vitro* and leads to higher toxicity towards cultured cells and cultured islets (33–36). A recent study suggests that S20G may undergo a different structural organisation during the fibrillation compared to the wildtype (37). For example, S20G hIAPP aggregation is not affected by the small molecule inhibitor YX-I-1, which inhibits aggregation of the wildtype

sequence (37). Studying the structural behaviour and the assembly of S20G may, therefore, provide novel insights into its enhanced amyloidogenicity and cytotoxicity.

1.2 The relevance of IAPP aggregation in Type II Diabetes Mellitus

Mature hIAPP is co-stored and released with insulin from β-cells, responding to signals that also trigger insulin release (38). IAPP helps modulate the pancreatic glucagon secretion from alpha-cells, inhibits gastric emptying and reduces eating. Food consumption leads to a rapid increase in circulating hIAPP, and it is known that exogenous hIAPP reduces eating soon after application (38). The effects of pancreatic hIAPP appear to be mediated in the central nervous system. Consequently, hIAPP analogues hold significant potential in treating metabolic disease and obesity (39, 40). Notably, the physiological concentration of hIAPP in granules far exceeds the threshold required for rapid amyloidogenesis observed *in vitro* (41, 42). This observation suggests intrinsic regulatory mechanisms within the secretory granules that inhibit IAPP aggregation under physiological conditions. Insulin, which is co-localized with IAPP, is postulated to be a key modulator of IAPP aggregation, along with the low pH environment of the granule (43). Studies indicate that soluble insulin can interact with IAPP, impeding its aggregation (44). However, within the granules, insulin exists in a semi-crystalline form complexed with zinc ions, complicating the extrapolation of these findings to an *in vivo* context (44–47). Additionally, the high concentration of zinc ions within the granules is also implicated as a potential inhibitor of hIAPP amyloid formation (48), but hIAPP-metal ion interactions remain incompletely understood and are an active area of investigation.

hIAPP amyloid deposition in the pancreatic islets of Langerhans is a hallmark of T2D, with pancreatic amyloid deposits reported in over 90 % of T2D patients (49, 50). Current research suggests that the toxic species are not the hIAPP fibrillar aggregates themselves but rather the soluble, lower-order oligomeric hIAPP intermediates that formed during the early aggregation (38).

These toxic hIAPP oligomers are implicated in cellular toxicity via various mechanisms that lead to β-cell damage and death, including membrane disruption (24, 38), mitochondrial dysfunction and oxidative stress (51), inflammation (52), endoplasmic reticulum (ER) stress (53), and activation of signalling pathways such as JNK, caspase cascade and the RAGE receptor (38, 52, 54–58). Aggregation of hIAPP to produce toxic oligomers likely also plays a key role in islet transplant failure and thereby may limit this treatment of type-I diabetes (59, 60).

1.3 IAPP Aggregation Pathways

The nucleation-dependent polymerisation model is a well-known model for describing protein aggregation that posits that the lag phase is characterised by structurally dynamic, transient, and heterogeneous oligomers. These oligomers can further associate to form higher-order oligomers, which can either serve as precursors of the amyloid in an on-pathway process or fail to assemble into amyloid fibrils in off-pathway events (61, 62). In the on-pathway scenario, nucleus formation is crucial for fibril elongation, which consequently facilitates rapid fibril elongation and marks the transition to the growth phase

(63). The growth phase culminates in the saturation phase where the amyloid fibrils reach equilibrium with soluble peptide (38). Models that include secondary nucleation, wherein the surface of IAPP fibrils serves a catalysis for the generation of new aggregates are required to describe IAPP amyloid formation *in vitro* (64, 65). As amyloid formation progresses on a complex energy landscape, minor variations in experimental conditions can lead to formation of different polymorphs which alter the aggregation pathways. Aggregation appears to be optimally explained by a model that includes secondary nucleation. Initially, the monomers aggregate into higher-order oligomer and fibrils via primary nucleation and elongation process. When the quantity of fibrils reaches a critical threshold, the surface of the existing fibrils plays a crucial role in promoting and accelerating further fibril elongation and new oligomer formation, as depicted in figure 3 (65). Camargo *et al.* demonstrated that the $t_{1/2}$ is linearly dependent on the logarithm of the fibril seed concentration, a key characteristic kinetic signature of an aggregation process involving a catalytic secondary pathway (66). The results presented by Camargo *et al.* are in good agreement with studies of other amyloid-forming peptides, such as Aβ and α-synuclein. Both of these polypeptides have been shown to undergo such secondary nucleation mechanisms (67–69). These theoretical and experimental studies underscore the complexity of hIAPP aggregation pathways and point out the importance of nuanced characterisation of the various oligomers and fibril seeds; such studies may shed light on the distinct mechanistic process of hIAPP aggregation.

Characterisation of oligomeric intermediates formed during hIAPP aggregation has been a key focus of research. Several studies have shown that depending on conditions, early oligomeric intermediates formed in the early aggregation stages are key toxic species (38, 58, 61, 62). These oligomers have been shown to induce β-cell death, while the mature hIAPP fibrils do not contribute to β-cell death *in vitro* (73, 74). Abedini *et al.* used time-resolved biochemical and biophysical assays to investigate the hIAPP oligomeric intermediates populated during the “lag phase” of amyloid formation (38). These oligomeric intermediates were found to be toxic, but mature amyloid fibrils were not. Camargo *et al.* showed that IAPP intermediate oligomers, rather than the mature amyloid fibrils represent the most toxic species *in vitro* (65). Consequently, a comprehensive molecular and structural knowledge of hIAPP oligomers is critical for studying hIAPP induced β-cell death and may pave the way to the development of targeted therapeutics.

1.4 Structural characterisation of IAPP oligomers

Efforts have been made to characterise the structure of hIAPP at each stage during its aggregation pathway in order to identify any structure-cytotoxicity correlations of hIAPP-induced β-cell death and T2DM disease progression. The aim is to describe key structural elements that are crucial for fibrillation. Studies using photochemically induced cross-linking have detected a distribution of hIAPP species ranging from monomers to hexamers, demonstrating that isolated hIAPP predominantly exists as low-order oligomers during the lag phase *in vitro* (38). This finding is further validated by Ion-mobility Mass Spectrometry (IM-MS) experiments (38). Circular dichroism (CD) has been used to demonstrate that hIAPP oligomers adopt helical structures (16, 17, 20, 75), a conclusion that is supported by isotope edited two dimensional infrared spectroscopy (2DIR) (70). Glodsbury *et al.* used CD

to monitor the *in vitro* aggregation of hIAPP and reported that the structure of hIAPP transits from a random coil to a β-sheet and α-helical structure prior to the final β-sheet fibrils formation (76). Later studies also reported the α-helical structure of hIAPP based on CD and 2D-IR (70). The comparative analysis of 2D-IR spectra between mature hIAPP fibrils and the hIAPP intermediates isolated during the lag phase indicates that the intermediates exhibit a lower level of β-structure (70).

The structure of hIAPP in the membrane-like environment is worth studying as one of the proposed toxicity mechanisms is via hIAPP-membrane interactions. A nuclear magnetic resonance (NMR) structure of hIAPP suggested a disordered C-terminus (77). A solution NMR study of the SDS micelle-bound hIAPP structure from Nanga *et al.*, however, demonstrated that hIAPP exists in a primarily α-helical conformation. This hIAPP structure is characterised by two helices spanning residues 7–17 and 21–28. These two helices are separated by a turn, resulting in a strongly bent structure and a helical C-terminus (78). Electron paramagnetic resonance (EPR) studies for micelle-bound hIAPP also reported the α-helical structure between residues 9–22 and no secondary structure at the terminal region (79). Other studies report that residues 20–22 of hIAPP adopted a fully helical structure to a lesser extent when bound to membrane or micelles (16, 77, 78). However, it is very important to note that the model membrane systems used in these studies are not good mimics of the β-cell plasma membrane as they usually lack cholesterol, have a simple lipid composition and a very high content of anionic lipids and lack membrane asymmetry.

Helical structure formation has also been observed in the Aβ peptide and α-synuclein, and has been proposed to affect amyloid fibril formation and toxicity (80, 81). These studies proposed a potential role of helical structure as a recognition factor for oligomerisation by acting as a seed for further oligomer formation by stabilising small β-sheet oligomers (82). In contrast to the challenges in characterising lowly-populated transient hIAPP oligomers in the early aggregation stage, hIAPP mature fibril structures have been studied by X-ray diffraction, solid-state NMR and cryo-EM (83–89).

Conventional bulk solution biophysical techniques report on the global averages of the species present and it can be difficult to deduce the contribution of individual types of oligomers and the role of inter- and intra-molecular interactions during the oligomerisation process. In addition, the transient and interconverting structural ensembles cannot be captured under native conditions (90). Single molecule studies can be performed, but these involve the labelling with dyes and the effects of the labels on aggregation may not always be benign and high-resolution structure information can be hard to obtain. Native Ion-mobility mass spectrometry (IM-MS) is, therefore, a promising technique for probing hIAPP structural dynamics under the native equilibrium of the ensemble (91). It is a powerful analytical method capable of isolating and differentiating transient and lowly-populated conformational families, requiring modest amounts of sample. IM-MS can thus provide a detailed conformational characterisation of hIAPP oligomers.

2. Ion-mobility Mass Spectrometry

Mass spectrometry (MS) is a powerful analytical technique that separates gas-phase analyte ions based on their mass-to-charge ratio (*m/z*), thus allowing the calculation of the analyte mass. When coupled with ion dissociation approaches, it can also elucidate the composition and structure of ions. The application of MS to biological macromolecules relies on the development of "soft" ionisation techniques, such as electrospray ionisation (ESI), that ionise biomolecules while preserving their structure and interactions with other biomolecules (92–94). The ionised gas-phase biomolecules are then separated in a mass analyser based on their *m/z,* and finally arrive at the detector where the ions are detected. Native MS employs nondenaturing and volatile solvents. Under tightly controlled pH, temperature and ionic strength conditions and the use of finely tuned instrumentation, native MS preserves the structures and interactions of proteins or complexes. Nowadays, nanoESI (nESI) is more widely used as it uses less sample and is more tolerant to salts compared to standard ESI. Different instruments, such as quadrupole ToF (QToF) and Orbitraps, have been commonly used in native MS studies (95).

Ion separation in IM-MS is based on their reduced mobility (K_0) in a drift tube filled with inert buffer gas. In the typical drift-tube ion mobility spectrometry (DTIMS), a constant electric field is applied to drive the ions through the buffer gas-filled drift tube to the detector, with ions continuously colliding with the buffer gas. Ions of the same mass and charge but differing in conformation will exhibit different reduced mobility: more extended conformers will encounter more collisions and arrive at the detector later, resulting in a longer drift time (Fig 4, Top panel). The ion-mobility dimension and the rotationally averaged collision cross section (CCS) values provided by IM-MS are beneficial for resolving the situation where different oligomeric states overlap in the *m/z* dimension, but can be separated using the IM dimension. For instance, consider a monomer with a +1 charge state (denoted as n/z, where n represents the oligomeric state and z the charge state) and a dimer with a +2 charge state (represented as 2n/2z). In mass spectrometry, the isotopic peak distributions for these species would converge in the same *m/z* region. This overlap poses a significant challenge, especially for lower-resolution mass spectrometry instruments, which lack the capability to provide a distinct isotopic distribution necessary for the unambiguous identification of different charge states. Another way of distinguishing between such monomer and dimer species is to compare their collision cross sections provided by IM. Assuming a spherical isotropic growth for these oligomers, the CCS (σ) of an oligomeric state n, can be described as $\sigma = \sigma_{mon} \times n^{\frac{2}{3}}$, where σ_{mon} is the CCS value of the monomer (96). Higher oligomers generally exhibit larger collision cross section values compared to monomers. Additionally, these oligomers often carry higher charge states, which are accelerated faster through the drift tube due to the stronger forces they experience. To comprehensively analyse the influence of both CCS and charge states on ion mobility separation and the drift time, ion mobility is frequently described by the collision cross-section-to-charge ratio (Ω/z) (97). In the above example, the dimer that carries twice the charge ($2n^{\frac{2}{3}}/2z$) will traverse the mobility cell faster than that of the monomer which carries a single charge ($1n/1z$) (Fig 4, Bottom panel). By incorporating an additional IM

dimension, IM-MS emerges as a powerful technique for the unambiguous differentiation of analytes in the gas phase, boosting the signal-to-noise and increasing confidence in molecule identification (98). By correlating CCS values with their *m/z* ratios, it has been shown that different classes of biomolecules – ranging from lipids, peptides, phosphorylated peptides, carbohydrates, and oligonucleotides – can be separated and identified, as they occupy distinct conformational landscapes (98, 99) (Fig 5 (a)). A similar trend also exists within each biomolecular class, IM-MS efficiently distinguishes isobaric species, such as leucine and isoleucine isomers (100), carbohydrate isomers (98), and lipid isomers (98), based on their conformational preference in gas phase.

The results of an IM-MS experiment are represented as the arrival time distribution (ATD). Gaussian peaks are often fitted to these ATDs to represent different conformational families (92). ATDs can be converted into the CCS either by calibration approaches (97, 99, 102), or via first principles (103, 104). The CCS can be considered the conformational envelope for a given protein in the gas phase (103). Experimental CCS values can then be compared with those calculated from structures or computational models (105). CCS values are, therefore, invaluable identification factors for differentiating proteins exhibiting different isomeric forms and structural dynamics (106).

Various IM methods have been introduced since the development of drift tube ion mobility spectrometry (DTIMS). These include differential mobility analysis (DMA) (109), travelling wave ion mobility spectrometry (TWIMS) (110), and trapped ion mobility spectrometry (TIMS) (111). Each method varies in its instrumental setup and in the way it measures reduced mobility and collision cross section (CCS) values. As previously mentioned, DTIMS applies a constant electric field across the drift tube, allowing CCS values to be calculated directly from the Mason-Schamp equation (112):

$$\Omega = \frac{3e\varkappa}{16N}\left(\frac{2\pi}{\mu k_B T}\right)^{\frac{1}{2}}\frac{1}{K_0}$$

Where Ω is the CCS, e is the elementary charge, $\varkappa$ is the analyte ion charge state, N is the density of the buffer gas, μ is the reduced mass of the collision, k_B is the Boltzmann constant and T is the absolute temperature in Kelvin. TWIMS, unlike DTIMS, creates an electrical wave which moves along the device (113). The electrical wave is achieved by a stacked ring ion guides (SRIGs). These alternate the electric field when the transient DC voltage is applied (110, 114). In TWIMS, ions with expanded conformations travel on the wave more readily than the compact ions, resulting in a longer arrival time. Obtaining the CCS from TWIMS is not possible through direct calculation from first principles, as in DTIMS (103, 104). Instead, it requires a CCS calibration using standards of known CCS values (115). Both DTIMS and TWIMS are known as *time-dispersive* IM-MS, as the mobility is reflected by the time taken to travel through the drift tube (116). *Spatially dispersive* IM-MS, such as differential mobility analysis (DMA) (117) and field asymmetric waveform IMS (FAIMS) (118), utilise the gas flow perpendicular to a modulated electric field, allowing the separation of ions into distinct regions based on their ion mobility. *Field-dispersive* IM-MS, including Trapped IMS (TIMS), uses a gating field and opposing gas flow to “trap” and

elute ions to traverse the drift region (119). These techniques provide different resolving power that can be tailored to each application. The growing popularity of using different IM-MS instruments is reflected in the exponential increase in publications on the subject (116).

The IM dimension can be indispensable in elucidating the structural evolution of oligomers. Typically, granular aggregates stem from isotropic growth of oligomers, while fibrils result from unidirectional growth (96). First described by Bleiholder et al., the differences between these two types of structural evolution can be distinguished by plotting the CCS value as the function of an increasing number of oligomeric states (Fig 5 (b)). As mentioned previously, the CCS (σ) of an oligomeric state n in isotropic growth, can be described as $\sigma = \sigma_{mon} \times n^{\frac{2}{3}}$, where σ_{mon} is the CCS value of the monomer (96). In contrast, the CCS values for ideal fibril growth form a linear relationship described by $\sigma = an + k$, where a and k are indicative physical parameters of the fibril shape. This CCS against oligomeric state method allows for the delineation and comparison of the growth and assembly mechanisms of the oligomers. Based on the CCS values provided by IM-MS experiments, this approach has been applied to study different amyloid systems (120, 121). Seo *et al.* integrated IM-MS with gas-phase infrared spectroscopy (IR) to study the structural evolution of amyloid-forming peptides VEALYL (87, 96, 120, 122). The derived CCS plot of VEALYL oligomers deviated from the trajectory of the ideal isotropic growth. This suggests a polydisperse and polymorphic nature of VEALYL oligomers (120). A recent study by Khaled *et al.* further demonstrated how IM-MS and CCS plots could resolve the shape of the growing Aβ oligomers (121), demonstrating that after isotropic tetramer formation, the CCS of further Aβ oligomers deviates from the isotropic models and forms an extended shape. Contrastingly, the truncated Aβ segment (Aβ1–28) that has the β-hairpin forming region removed forms oligomers with CCS values that are more relevant to the ideal isotropic model. Hence, by utilising experimental CCS values, IM-MS helps distinguish the shapes of oligomers, providing crucial structural insights into their aggregation assembly mechanism.

IM-MS offers several advantages that are particularly useful for studying protein systems like IAPP. The use of IM-MS can sample the entire conformational landscape, making it ideal for studying proteins that co-exist in multiple conformations and are transient, such as intrinsically disordered proteins (123). IM-MS is also widely used in biotechnology settings, providing a detailed characterisation of the kinetics, structural changes, and stability upon drug binding (97).

Ion activation methods, whereby the internal energy of an ion is intentionally increased prior to IM-MS analysis, have been used to reveal the structural dynamics and the gas-phase stability of ions (124–126). Early injection energy studies increased the energy by which ions enter the IM-MS device, and were used to probe the unfolding of a number of model and disease-related proteins (89, 106, 107) Collision induced dissociation (CID), which is most commonly used to fragment the peptides when applied to proteins or protein complexes, induces the unfolding of the protein, in a process commonly termed collision induced unfolding (CIU) (129). CIU has been extensively applied to compare the tertiary structure, gas-phase stability and ligand binding of protein complexes (125, 130–133). These

methods, typically visualised through IM-MS driftscope plots and CIU fingerprint heatmaps – alongside the aforementioned CCS-related plots, have emerged as powerful tools for studying protein structure and dynamics, unfolding and aggregation of antibodies, Aβ, β-2 microglobulin, and viral capsid assembly (96, 108, 134, 135). A driftscope plot presents a two-dimensional mapping of arrival time versus mass-to-charge (*m/z*) ratio, with each point designating a detected ion (Fig 5 (c)). It has been widely used in identifying protein binding interactions, including antibody conjugation and small-molecule drug binding (107). Debaene *et al.* demonstrated the use of native IM-MS to characterise antibody drug conjugates by the comparison of the driftscope plot of drug loading on brentuximab vedotin to the unconjugated monoclonal antibody brentuximab (107). This allows a rapid assessment of antibody drug conjugate structure, binding stoichiometry, and conformational changes (107). In IM-MS, the heat map fingerprints can be generated through collision activation experiments that use increasing collision energy to reveal how protein structures unfold and disassemble, as shown in Figure 5(d). The heat map depicts the arrival time distribution at each collision energy, reflecting how ion mobility and, consequently, the CCS value, increases as the protein unfolds with increasing internal energy. IM-MS-derived heat maps are now widely recognised as the fingerprint profile for protein structural stability, aiding the discovery of structural intermediates (136), assessing polydispersity (137), ligand binding or protein conformational variations (138). Furthermore, these IM-MS data have provided a fruitful resource compatible with computational modelling in biophysics and structural biology. The CCS values and energetic profiles obtained by IM-MS serve as a structural envelope, or the constraints can be used to validate or refine structures modelled by computational methods such as molecular dynamics (MD) or docking experiments. Work by Biehn *et al.* has developed a scoring model which utilises IM-MS CCS data to improve the protein tertiary structure prediction by penalising the difference between the CCS values of the predicted structure and the experimental CCS values available (139).

Relatively recent work has combined gas phase spectroscopic measurements with IM-MS. These methods combine the exquisite ability of IM-MS to separate and trap species with structural methods that provide more detailed information than CCS values. Both gas phase IR and gas phase Fluorescence energy transfer (FRET) have been incorporated with IM-MS. By integrating gas phase IR with IM-MS, ionised species can be selectively analysed through mass and ion-mobility dimensions, and their secondary structure can be probed (140–143). IR is well known to be sensitive to secondary structure in solution and the amide-I mode, primarily a C=O stretch, is widely used to study secondary structure. The density of ions in the gas phase is normally too low to perform absorption IR measurements, instead the spectrum is mapped out indirectly. In one method, the sample is irradiated with a high energy pulse of IR photons resulting in multiphoton absorption provided the IR radiation is resonant with an IR active mode. The multiphoton absorption leads to fragmentation which can be detected by MS. Thus, by using a tuneable IR source and monitoring the amount of fragmentation produced as a function of wavelength an IR “action spectrum” can be obtained. The IR action spectrum obtained does not have to match that of a conventional IR absorption spectrum. The addition of IR to IM-MS allows for the identification and validation of unique structural elements within the oligomers, providing further evidence for their structural evolution. To date the method has been applied to study

the aggregation of small peptides derived from insulin and from IAPP as well as a fragment of Aβ (120, 121, 144). The intense IR source required, a free electron laser, means the technique is specialised and to date has been applied by a few labs only. IR spectra of gas phase ions can also be measured using infrared predissociation spectroscopy of cold ions and this avoids the use of free electron lasers (145, 146).

Fluorescence energy transfer (FRET) has also been interfaced with mass spectrometry, including with IM-MS (147). In FRET, a donor fluorophore and an acceptor fluorophore are conjugated to the protein or biomolecule of interest (in some cases, intrinsic fluorophores can be exploited). The donor absorbs photons of a specific wavelength, and if the donor-acceptor distance is small enough, radiationless energy transfer occurs, provided, there is an overlap between the emission spectrum of the donor and the absorption spectrum of the acceptor. If these conditions are met, red-shifted fluorescence emission from the acceptor is detected. The intensity of the FRET signal is sensitive to distance, varying as one over the sixth power of the distance, and FRET has been widely applied as a "molecular ruler" in solution experiments and used to monitor the proximity of biomolecules *in vivo* (148). FRET is challenging to carry out in the gas phase because, like with IR, the low ion population that is trapped makes optical measurements difficult. Dugourd and coworkers developed "Action FRET" to overcome these difficulties (149). In this measurement dissociation of the acceptor chromophore and parts of the biomolecule near the acceptor are used to monitor the FRET signal and probe the proximity of the donor and acceptor, Action FRET avoids many of the difficulties of optically detected FRET since fragmentation products are detected instead of light many of the sensitivity problems of optically detected FRET from stored gas-phase ions can be avoided. The method has been applied to Aβ peptides and to intact globular proteins (150–152). Action FRET does require measurements at many wavelengths to cover the absorption bands of both donor and acceptor. Optical detection overcomes this technical complication. Optical detection of FRET of trapped ions has also been developed and combined with MS and has been recently reviewed by Nielsen and coworkers (153). The combination of FRET and IR with IM-MS holds great promise and as instruments become more accessible should have a significant impact on studies of amyloid aggregation.

Given the advantages that IM-MS offers, it is unsurprising that it has been extensively applied to study the structural dynamics of hIAPP, as well as to understand hIAPP aggregation and its correlation with the hIAPP amyloid-induced β-cell toxicity. This review summarises the application of IM-MS in elucidating the mechanisms of hIAPP amyloid formation and its interactions with ligands and small molecules, demonstrating the benefits of using IM-MS in this field. Furthermore, the review discusses the future potential of recent developments in ion mobility instrumentation, notably the development of tandem IMS instrumentation, to address and overcome the current challenges in studying hIAPP amyloidogenesis and cytotoxicity.

3 Investigation of hIAPP Aggregation through IM-MS

3.1 hIAPP intrinsic amyloidogenicity: An IM-MS perspective

Molecular dynamics (MD) simulations and experimental studies, have revealed the aggregation capability of IAPP fragments (154). The self-aggregation of IAPP has sometimes been attributed to the intrinsically "amyloidogenic domains" within its sequence, particularly the region spanning from 1–8 ($K_1CNTA_5TCA_8$), 20–29 ($S_{20}NNFGA_{25}ILSS_{29}$, which has been known as the "amyloidogenic core") and a fragment from the C-terminal $S_{28}STNVG_{34}$ region (96, 154–156). Although the situation is more complex in the intact molecule, the study of peptide fragments can provide useful insights and was an important early step in studies of hIAPP amyloid formation. The characterisation of individual "amyloidogenic domains" may also facilitate the identification of targets for therapeutic intervention. However, it is important to note that there is not a single amyloidogenic domain in hIAPP and peptide fragments of hIAPP are usually slower to aggregate than the full-length polypeptide when studied at similar concentrations. While the aggregation mechanism of small peptide fragments may mimic that of the full-length polypeptide it does not have to. Owing to the sensitivity of IM-MS, it is ideal for monitoring detailed conformational changes and the potential formation of transient and heterogeneous oligomers for those IAPP fragments and full-length hIAPP with similar masses.

3.1.1 hIAPP fragments landscape: N-terminus to C-terminus aggregation profiles—

The hIAPP N-terminus region ($K_1CNTA_5TCA_8$, residues 1–8) contains a disulphide bond between Cys2 and Cys7 that has been reported to contribute to IAPP structural and functional activities *in vivo*, thus making the N-terminal region studied for IAPP function (157, 158). The isolated N-terminal segments have been studied, and different oxidation states of the disulphide were subjected to IM-MS studies in an effort to understand how the disulphide bond contributes to the IAPP oligomer formation and further aggregation (154). Ilitchev *et al.* prepared three forms of the hIAPP N-terminal peptide $K_1CNTA_5TCA_8$: the wildtype (oxidised) 1–8 fragment, the reduced 1–8 fragment that lacks the disulphide bond, and a cysteine-to-serine mutant for IM-MS analyses (154). Mass spectrometry indicated oligomer formation up to heptamers for all three species under physiological pH, making it challenging to discern the disulphide bond's role in aggregation based on studies of these fragments (154). Differences emerged, however, in the arrival time distributions (ATDs) and corresponding collision cross-section (CCS) values (Fig 6). The oxidised fragment was observed to form fewer higher-order oligomers, and adopted a much more compact conformation in its lower-order oligomeric state, whereas the conformation of its higher-order oligomers was more extended than those of the reduced and the mutant form (154). Atomic Force Microscopy (AFM) images showed that wildtype oxidised fragments formed larger globular aggregates upon seeding with fibrils formed by full-length hIAPP, whereas the reduced and mutant, formed more compacted structures. MD results revealed that the compacted structures contained higher intermolecular hydrogen bonding (154). Collectively, the application of IM-MS showed that the presence of an oxidised disulphide bond in the N-terminal region may reduce IAPP aggregation, with fewer higher-order assemblies observed. The CCS values also suggested that the disulphide bond may provide structural constraints by reducing intermolecular hydrogen bonding and β-strand structure

formation during lower-order oligomer formation. Independent studies of full length hIAPP in solution showed that the disulphide plays a role in slowing amyloid formation *in vitro* (159).

The 20–29 region of IAPP, S_{20}NNFGA$_{25}$ILSS$_{29}$, also proposed to be the "amyloidogenic core" (23), has been observed to form a β-sheet structure spanning the residues 23–27 during the fibrillation process, indicating the importance of this region in aggregation (23). Earlier studies have shown that the hIAPP$_{20–29}$ segment can form amyloid in isolation (23, 24). Thus, fragments of this region have been extensively studied using IM-MS-based methods to probe the intrinsic aggregation propensity of these regions of the sequence (160, 161). The fragment N_{22}FGAIL$_{27}$ is the shortest hIAPP sequence known to form amyloid fibrils at near physiological pH and is toxic to pancreatic cell lines (162). It has been hypothesised that oligomerisation of this fragment may arise from the hydrophobic interactions that further evolve into amyloid fibrils composed of antiparallel β-strands (162, 163). In contrast amyloid structures formed by full length hIAPP all contain parallel β-strands. Hoffmann *et al.* demonstrated that the N_{22}FGAIL$_{27}$ fragment undergoes a nucleation-dependent aggregation mechanism using IM-MS to monitor the conformational changes during aggregation (164). The mass spectrum of N_{22}FGAIL$_{27}$ showed a wide distribution of oligomers, from single-charged monomers to quadruple-charged 13-mers (164). The IM-MS data further showed that various conformations and higher oligomeric states of the same *m/z* value exist. The structures of oligomers, starting from tetramers as reported with the CCS values, ranged from compact to highly extended structures. For instance, the CCS values corresponding to +3 pentamers have compacted species with a CCS of 520 Å^2 and more extended species with a CCS of 540 and 566 Å^2. This trend of co-existing compact and extended conformers within the same oligomeric state was consistent for higher oligomeric states (hexamer to decamer), but not for lower-order species (164). The conformational data provided by IM-MS suggested that the N_{22}FGAIL$_{27}$ tetramer may be the point of structure transition towards a more partially folded, presumably β-sheet-rich structure. IM-MS and thioflavin-T (ThT) fluorescence data for the 8–20 fragments also reported that β-sheet-rich structures begin at the level of tetramer (165). IR measurements of this peptide also proposed the existence of a turn-like structure in lower-order assemblies, with extended β-sheet-rich structures becoming prominent in tetramers to 10-mers. A similar structural transition has been reported for several amyloid-forming proteins (96, 164). Overall, IM-MS efficiently demonstrated the conformational transition of the N_{22}FGAIL$_{27}$ from a turn-like and/or unordered structure to β-sheet-rich oligomers during on-pathway aggregation, indicating that such conformational transitions may be a signature feature of amyloidogenic proteins.

The IM-MS study focusing on the S_{28}STNVG$_{33}$ fragment led to a self-assembly pathway that contrasts the aforementioned structural transition to the extended β-sheet structure during the very early aggregation stage. Bleiholder *et al.* demonstrated that IM-MS could unambiguously reveal the isotropic oligomers formed by S_{28}STNVG$_{33}$ fragments (96). The CCS values indicated that S_{28}STNVG$_{33}$ self-assembles through orientationally isotropic compact oligomers until the "steric zipper" motif of two interdigitated extended β-strand appears at the undecamer stage (96). The study presented an aggregation model for S_{28}STNVG$_{33}$, where initial isotropic oligomerisation precedes before fibrillar structure

formation, with a pivotal transition with two extended β-strands emerging at oligomers of 12 or 14 $S_{28}STNVG_{33}$ subunits. AFM images showed granular structures resulting from isotropic aggregation and fibrillar aggregates resulting from β-sheet-rich fibril development (96). The results presented in that work, along with those from the previously mentioned studies on IAPP fragments, suggest that these IAPP fragments may not be the sole determinants of amyloid formation. The use of isolated IAPP fragments may represent an oversimplified model of the aggregation processes of full-length IAPP, especially when considering *in vivo* behaviour.

3.1.2 Full-length hIAPP: From monomers, dimers to higher-order oligomers

—The aggregate-forming capability of individual small peptides derived from aggregation prone regions of hIAPP has been demonstrated with IM-MS, but the behaviour of the full-length hIAPP may present a more complex scenario. IM-MS and molecular dynamics (MD) simulations have been used for the structural characterisation of full-length hIAPP monomer, dimer and higher-order oligomers (155, 166).

In important early work the +4 charge state of full-length hIAPP monomer identified by Dupuis *et al.* contains two structural conformers with CCS values of 770 $Å^2$ and 653 $Å^2$ (155). These conformers matched extended β-strand and compact helix-coil structures derived from the MD simulations. The extended β-hairpin structures of this +4 charge state hIAPP and non-amyloidogenic rIAPP were compared using IM-MS and MD. The extended β-hairpin secondary structure is significantly less pronounced in rIAPP, highlighting that the formation of the proposed β-hairpin is essential in amyloidogenic hIAPP. This extended β-hairpin structural feature may stabilise the hIAPP for further oligomerisation (155). Similar structures have been proposed for other amyloid-forming proteins, such as α-synuclein and Aβ (121, 167, 168). These proteins, including hIAPP, have been shown to bind to an affibody that recognises β-hairpin structures, indicating a shared conformational preference among these amyloidogenic proteins (167). The extended β-hairpin-rich hIAPP conformers, derived from MD simulations and CCS measurements by IM-MS, underscore the role of β-hairpin formation in advancing hIAPP towards further aggregation and fibril formation. This finding further underscores the effectiveness of IM-MS in refining hIAPP aggregation models.

Following the observation of the extended proposed β-hairpin conformation in hIAPP monomer, IM-MS was used to probe the role of this structure in the dimerisation of IAPP (166). Comparing the ATDs of the +5 dimer for hIAPP and rIAPP, it was evident that the hIAPP dimers at +5 charge states adopted a more elongated conformation with the CCS value of 1150 $Å^2$, whereas the rIAPP dimer displayed a more compact conformation with the CCS value of 1033 $Å^2$. The difference suggests the contribution the higher β-sheet content has in the extended hIAPP dimers. The MD analysis revealed that the extended β-strand conformation successfully recruited the coil region of the monomer during the dimerisation, transitioning the coil monomer into a β-strand at the monomer-monomer interface (166). The conformations identified by this IM-MS study suggest an aggregation pathway that may involve the early conformational transition into an extended β-strand conformer rather than the initial formation of helix-rich oligomers, which are followed by the β-sheet oligomers in later aggregation stages (166, 169, 170). It is interesting to

compare the IM-MS results to time-resolved solution studies. Bulk solution studies using time resolved two dimension IR methods in combination with specific 13C18O labelling suggest that α-helical structure is formed early in aggregation, as do CD studies, and that a key oligomeric species containing intermolecular parallel β-sheet structure is formed (82, 160, 171).

Young *et al.* utilised IM-MS to demonstrate the formation of hIAPP oligomers up to hexamers of hIAPP soon are dissolving the peptide at pH 6.8 (169). rIAPP was observed to form similar higher-order assemblies as hIAPP, indicating that the formation of oligomers does not always lead to amyloid fibril formation and implying that the properties//structure of the oligomers are important. The CCS values revealed that hIAPP consistently adopted a more extended conformation that occupies a larger population since the early aggregation stage (169). The distinction in the conformations of these two species highlights again the potential involvement of the extended conformation in hIAPP early state aggregation formation. A gas-phase stability comparison of the hIAPP and rIAPP oligomers was performed by subjecting the oligomers to increasing collision energies and suggested that the reduced gas-phase stability of early hIAPP oligomers is linked to amyloidogenicity. The reduced gas-phase stability is consistent with the observation that hIAPP oligomers are destabilised at higher ionic strength, presumably due to the lower structural stability of these early-stage transient oligomers, which predisposes them to sample and adopt amyloidogenic conformations (169).

3.2 IM-MS links the structural dynamics of aggregation to the toxicity in full-length hIAPP

After establishing that both hIAPP fragments and full-length molecules can form higher-order oligomers detectable by IM-MS, attention shifted towards understanding the effect of specific residues on full-length hIAPP amyloidogenicity and cytotoxicity. The development of Pramlintide, an IAPP analogue for treatment inspired by the non-amyloidogenic rat IAPP which differs from hIAPP at key residues including three proline substitutions, still faces solubility challenges and pH-dependent oligomerisation. These characteristics of Pramlintide have been shown by IM-MS and ThT fluorescence studies (172). This underscores the need for new hIAPP analogues and a deeper understanding of the impact of the specific residues on hIAPP aggregation and cytotoxicity. IM-MS is crucial in this pursuit, enabling detailed comparisons of hIAPP variants conformational properties and establishing links between structural properties, amyloidogenicity and cytotoxicity. The valuable information provided by IM-MS experiments will be vital in guiding the development of effective analogues with therapeutic applications.

hIAPP is not only able to form amyloid, but it also induces β-cell dysfunction and cell death. Comparative analyses of hIAPP sequences with IAPP sequences from other species, such as rat IAPP, bear IAPP and sheep IAPP, have revealed some key residue substitutions in hIAPP that may be important for its amyloidogenicity and toxicity (173). Ridgway *et al.* employed IM-MS as part of their studies of the amyloidogenicity and toxicity changes in hIAPP due to the proline substitutions found in rat IAPP, including $IAPP_{A25P}$, $IAPP_{S28P}$, $IAPP_{S29P}$ and double proline substitutions $IAPP_{A25P\ S28P}$, $IAPP_{A25P\ S29P}$ and $IAPP_{S28P\ S29P}$ (30). In that

study, S28P was shown to have a significant role in reducing amyloid formation and toxicity (Fig 7 (A)(B)).

IM-MS studies of these peptides measured the tendency of the IAPP analogues to form lower-order oligomers. The mass spectra showed a mixture of monomers and dimers reported for all proline analogues (Fig 7 (C)) with some higher-order oligomers also observed (30). Unlike the significant differences in toxicity observed in proline analogues, the CCS values for these hIAPP variants were shown to be very similar, but with notable differences, primarily in the +4 monomers and the +5 dimers. All hIAPP variant +4 monomers have two conformations: extended and compacted. Notably, the extended +4 monomer of $IAPP_{S28P\ S29P}$ showed a reduction of ~8–9% in the CCS value compared to the counterparts, indicating a more compacted monomeric structure. As for the dimers, only $IAPP_{A25P\ S28P}$, and $IAPP_{S29P}$ were reported with a single conformation, instead of two conformations reported for other peptides. Previous MD studies proposed the S28P substitution may promote the stabilisation of the local helical structure and delay aggregation by preventing the extended β-sheet structure formation (174, 175). However, the proposed S28P effects on compacting the IAPP monomer were not observed in this IM-MS study.

The intensity-weighted standard deviation of the CCS distribution ($IWSD_{CCS}$) serves as a complementary metric to monitor protein unfolding in collision-induced unfolding (CID) experiments. Ridgway *et al.* used the $IWSD_{CCS}$ metric to describe the extent of unfolding by detecting changes in CCS, thereby characterising the structural properties of IAPP (101). While all monomers showed similar $IWSD_{CCS}$ values, the dimers varied, with the $IAPP_{A25P}$ dimer exhibiting a notably wider CCS distribution (30). This suggests a unique unfolding behaviour for the $IAPP_{A25P}$ dimer. No apparent relationship could be established between the CCS values or $IWSD_{CCS}$ of the analogues and their tendency for amyloid formation, and cellular toxicity could be established based on the results. No detectable relationship was derived between the extended conformers and the abundance of the dimer or monomer populations with the solution T_{50} for amyloid formation and or the EC_{50} of toxicity (30). Perhaps the important transient and low-populated structural features are not discernible in monomer and dimer conformations or are too subtle for current CCS measurements. It is also possible that they are not correlated with toxicity and the rate of amyloid formation. Future advancements in high-resolution IM-MS and tandem IM-MS techniques will help resolve populations with similar CCS distributions more effectively, and the combination of IM-MS with spectroscopic measurements should yield finer structural insights to inform the relationship between hIAPP amyloid structure and toxicity. Thus, there are clearly many fruitful opportunities for future IM-MS studies of hIAPP aggregation.

3.3 Probing the interaction of metal ions with IAPP and their role in IAPP aggregation

The interplay between metal ions and hIAPP and amyloid formation is complex. A recent review by Alghrably *et al.* discussed how metals such as copper (Cu), zinc (Zn), aluminium (Al) and iron (Fe) are associated with amylin aggregation and T2DM (176). Zinc ions are notably abundant in pancreatic β-cell insulin secretory granules. The balance of zinc to hIAPP ratio in the β-cell granules may be crucial in maintaining hIAPP in its physiological

functioning state, while the disruption of this concentration balance may possibly be linked to hIAPP aggregation. However, the intragranular environment is complex. Although Zn ions are present at high concentration, the bulk of the Zn ions are associated with insulin and the insulin Zn complex forms a dense semi-crystalline core, the so-called dense core of the granule. hIAPP is found in the periphery of the granule, the halo-region. The halo region also contains soluble C-peptide, derived from the processing of insulin and other ions in addition to Zn (177). Thus, translating the results of *in vitro* experiments in buffer can be difficult. Further complicating the analysis, the effects of Zn^{2+} can be bimodal. Ramamoorthy, and coworkers have shown that low concentrations of zinc delayed hIAPP aggregation at physiological pH, but high concentrations of zinc enhanced aggregation (178).

In terms of copper ions, reports conflict on whether copper ions suppress or exacerbate hIAPP amyloid formation and toxicity, making the impact of copper ions in hIAPP conformational changes debatable (176). Several experimental approaches, including mass spectrometry, atomic force microscopy (AFM), X-ray photoelectron spectroscopy, and NMR have widely been used to investigate interactions between different metal ions with hIAPP (179). A comprehensive review by Moracci *et al.* provides an exhaustive summary of findings from these methodologies concerning the interplay between metal ions and hIAPP (180). For the purposes of this review, we specifically focus on studies employing IM-MS. IM-MS stands out for its unique ability to examine detailed IAPP-metal ion binding stoichiometries and elucidate the effects of these binding events on the conformational landscape of IAPP.

3.3.1 Rapid assessment of copper ion inhibition of hIAPP aggregation via IM-MS—

A previous study incorporating mass spectrometry, solid-state NMR and computational simulations indicated that copper (II) instigates notable structural changes in hIAPP leading to a preference for a compact conformation, which in turn decreases the progression towards oligomer formation. This change in structural equilibrium is also evidenced by changes in hydrogen exchange kinetics and limited proteolysis experiments confirmed by MALDI-MS, pinpointing the His-18 region as the potential primary copper binding site (181).

The intricate interactions between copper ions and hIAPP and their effects on hIAPP aggregation and conformation have been studied using ion mobility separation (IMS) in conjunction with laser ablation electrospray ionization mass spectrometry (LAESI-MS). LAESI-MS is an ambient ionisation technique that combines laser ablation from a mid-infrared laser to generate gas-phase ions via the interactions with charged particles in electrospray (182). Integrating LAESI with IM-MS provides an additional benefit for studying noncovalent complexes in their more native state (183). Research by Li *et al.* has shown the effectiveness of LAESI-IMS-MS in elucidating the binding stoichiometry, metal ion oxidation state and binding kinetics of the hIAPP-Cu^{2+} complex, as well as tracking the changes in hIAPP conformation induced by the Cu^{2+} interaction (184). When hIAPP was incubated with Cu^{2+}, the LAESI mass spectrum revealed the formation of hIAPP-Cu^{2+} complexes in +5, +4, and +3 charged states, each binding with a single Cu^{2+} ion. The copper in these complexes was confirmed to be in the +2 oxidation state, and no reduction to the

+1 state was observed. This was determined from the isotopic peak distribution analysis in the mass spectrum for the +5, +4 and +3 charged hIAPP-Cu^{2+} complex ions. Tandem mass spectrometry was used to identify the preferred copper-hIAPP interacting sites. To identify the copper ion binding site in hIAPP, Collision-Induced Dissociation (CID) was performed on both the +4 hIAPP ions (*m/z* 976.233) and the copper-bound hIAPP complex [hIAPP–Cu^{2+}+2H]$^{4+}$ (*m/z* 991.459). The CID fragmentation pattern of the copper-bound +4 complex revealed the presence of b25 and b26 fragments, which are consistent with the fragmentation pattern of the +4 hIAPP ions. The notable absence of b17 fragments in the CID spectrum of the [hIAPP–Cu^{2+}+2H]$^{4+}$ ion implies that t amino acid residues 18–25 (–H_{18}SSNNFGA$_{25}$–) are likely the copper coordination site (184). This result aligns with the findings from the limited proteolysis experiments and MS analysis of Sinopoli *et al.* (181).

IM-MS has been utilised for its exceptional capacity to differentiate between hIAPP conformations, detecting changes and potential oligomerisation resulting from copper binding. In the absence of copper binding, IM-MS discerned two conformers for +3 monomeric hIAPP with CCS values of 611.2 $Å^2$ and 646.5 $Å^2$. These two experimentally detected conformations are assigned to the same structures derived from the simulations: one simulated in a solvent-free vacuum, and the other, a β-sheet-rich structure, resulting from a simulation that eliminated all water molecules followed by energy minimisation. For the +4 monomeric hIAPP ions, two conformers with CCS values of 594.2 and 747.8 $Å^2$ were also assigned to the solvent-free conformation and the long β-hairpin structure conformation, respectively (155). The deconvoluted drift time (DT) distribution indicated that the favoured conformations of +3 hIAPP and +4 hIAPP monomeric ions were distinct, with the β-sheet rich structure being more abundant in the +3 hIAPP ions, while the other structure was dominant in the +4 hIAPP ions. Following this, IM-MS was then applied to ascertain the CCSs values of +3 and +4 hIAPP ions in the presence of Cu^{2+} complexation (184). The measured CCSs value for the +3 and +4 charged hIAPP-Cu^{2+} complexes exhibited almost identical CCSs values with the +3 hIAPP ions, suggesting that the Cu^{2+} binding does not significantly change the hIAPP conformations. Nonetheless, subtle variations in the conformer abundance were still noted, which may offer further insight into to the preferential biding sites mentioned above.

The use of LAESI-IMS-MS enables rapid and high-throughput analysis of copper-hIAPP complex formation and the changes in oligomerisation of hIAPP. IM-MS facilitates the examination of the detailed conformations of hIAPP across different charge states by utilising collision cross-section (CCS) values. It also provides evidence supporting the inhibitory role of copper in the formation of IAPP oligomers, potentially by disrupting β-sheet formation in the critical His18 region.

3.3.2 IM-MS identifies the hIAPP conformational transitions induced by Zinc

—Under physiological conditions, zinc exists in millimolar concentration within the secretory granule, playing an essential role in packaging of insulin into insulin granules and storing it into the dense core. Two zinc ions are required per insulin hexamer, which eventually results in the high millimolar concentration of zinc in the secretory granule. Although zinc ions interact directly with insulin under physiological conditions, they are also known to modulate hIAPP aggregation *in vitro* through coordination with hIAPP (46,

185, 186). Several independent groups have reported that hIAPP aggregation inhibition could be observed only at intermediary zinc concentration, whereas either very low or very high zinc concentration could enhance hIAPP aggregation (48, 178, 187). Collectively, the complex roles of zinc in hIAPP aggregation promotion or inhibition and the corresponding concentration condition await further clarification. This particularly includes the detailed structural characterisation of the hIAPP early oligomers under varying zinc concentrations.

Ilitchev *et al.* have elucidated the conformational transition of hIAPP in response to different zinc concentrations using IM-MS (188). A concentration-dependent effect of zinc on hIAPP aggregation was reported in this study. The mass spectrum revealed that the hIAPP monomer with a +4 charge state shows the highest level of zinc association. This strong association is presumed to occur because zinc typically carries a +2 charge and can add an extra charge to the native +3 charge state monomer. Initially, at lower zinc concentrations, hIAPP begins to bind with a single zinc ion, and hIAPP+Zn^{2+} predominates. As the ratio of zinc: hIAPP reaches 10:1, adducts in the form of hIAPP+$Zn(H_2O)_5^{2+}$ are observed. Increasing the relative zinc concentration to 25:1 results in hIAPP attaching to two of these hydrated zinc ions, forming hIAPP+$2Zn(H_2O)_5^{2+}$. No forms of hIAPP binding to two zinc ions without hydration or a combination of hydrated and non-hydrated zinc ions were detected.

The ATD profiles from IM-MS analysis under varying zinc to hIAPP ratios, ranging from 1:1 up to 100:1, indicate a transition in the structure of Zn-hIAPP adducts. The Zn-hIAPP adduct shifted from the compact conformer (648 $Å^2$) to an extended proposed β-hairpin form (746 $Å^2$), which was identified as the amyloidogenic conformer. This effect is even more prevalent with higher zinc concentrations. It is worth mentioning that the proposed extended β-hairpin conformer of hIAPP is uniquely found in the amyloidogenic species and has been proposed to be a the precursor for the toxic hIAPP oligomers (155, 166, 189, 190). The results, described in Figure 8, underscore the potential role of zinc ions in promoting the formation of these species. In this model, single zinc or penta-aqua zinc's promotion of the putative extended β-hairpin conformation, likely through attachment at H18, destabilises the helix-coil state. Thus, targeting this conformational shift might be a therapeutic approach to prevent the formation of harmful hIAPP oligomers. Further validation by AFM analysis indicates that low concentrations of zinc, especially the hydrated form promote the aggregation of the structure. However, at moderate zinc concentration, when more hIAPP forms adducts with Zn^{2+} or $2Zn(H_2O)_5^{2+}$, the complexes inhibit the transition to β-sheet oligomers and proto-fibrils (188). A decrease in the proto-fibril formation is observed with zinc ions stabilising the extended structure when the relative zinc concentration is above 50:1 Zn^{2+}:hIAPP. Indeed, the ATD of anhydrous zinc-hIAPP complex, on the other hand, shows that anhydrous zinc favours β-hairpin conformation less than the hydrated form (Fig 9), highlighting the role of ligand waters in the stabilisation process. Overall, the IM-MS studies in combination with AFM, highlighted the complex role of zinc in hIAPP, showing the concentration and hydration state of zinc greatly influencethe hIAPP conformation transition. The binding of zinc to hIAPP, influenced by its hydration state, can favour the formation of a stable amyloidogenic conformation, but inhibits the aggregation into toxic oligomers primarily when hIAPP-Zn^{2+} is the dominant component in the complex. This study also makes a cautionary note that merely observing the conformational preference

for the proposed β-hairpin or other potential oligomer precursors may be inadequate to conclusively determine the amyloidogenic pathway of hIAPP.

hIAPP metal ion interactions are complex, and there is clearly more to be learned. IM-MS studies of hIAPP metal ion structure are a developing field and hold the promise of providing additional insight into these complex processes and complication solution phase investigations.

3.4 IM-MS in monitoring IAPP hetero-oligomerisation

In addition to metal ions, the presence of other amyloid-forming peptides alongside IAPP adds complexity to hIAPP aggregation within the cellular environment (191). *In vitro* amyloid formation by hIAPP is commonly and extensively investigated using single purified proteins, but co-polymerisation of hIAPP with different amyloid-forming proteins, such as Aβ, involved in Alzheimer's disease is likely to occur *in vivo*. This interaction may impact the rate of the fibril formation and pathogenicity of the resulting co-assembly (169, 191, 192). IM-MS is particularly effective in detecting the heterogeneous and sparsely populated species that arise from the potential interaction between IAPP and other amyloid-forming peptides. This capability enables the study of hIAPP co-polymerization with these peptides and provides detailed information on oligomer composition and conformation.

Previous studies have shown that WT hIAPP and rIAPP can co-polymerise to form mixed amyloid fibrils, but the assembly rate changes were insignificant (169, 193, 194). Cross-seeding is a proposed mechanism where the precursor peptide sequences act as a "seed" to enhance further fibril growth of variant peptides by templating the precursor's structure. Fibrillation induced via cross-seeding mechanism has an increased fibrillation rate and has a distinct structure formed *de novo* (195–197). Young *et al.* used ESI-IM-MS combined with measurements of fibrillation rates using ThT fluorescence to show that hIAPP can form hetero-oligomers consisting of various IAPP variants. Their results also demonstrated polymerisation of IAPP sequences changes the amyloid assembly rate by altering the conformational properties of the hetero-oligomers formed (198).

Young *et al.* studied mixtures of WT hIAPP with IAPP variants (rIAPP, H18L-HIAPP, S20G-HIAPP, I26P-hIAPP, and hIAPP with a free C-terminus) to explore their self-assembly, co-assembly abilities and any alterations in amyloid formation rates (198). The mass spectrum of WT hIAPP primarily displays monomers and also oligomers to hexamers, consistent with previous observations (169, 199). rIAPP and the IAPP variants that form amyloid more rapidly (H18L and S20G) or more slowly (FreeCT) all show a comparable mass spectrum pattern in monomer charge states distribution and traces of oligomers of dimer to hexamer (Fig 10). I26P-IAPP, on the other hand, displayed the slowest oligomer formation and had a change in the monomer ions charge state distribution. The ratio of +3: +2 monomer ions of I26P changed to ~3: 1, which is a similar ratio observed for WT hIAPP in the presence of small molecule inhibitors. This change in ratio suggests that the change in the amyloid formation capacity induced by the I26P mutation could result via potentially disrupting amyloid-competent conformations (169, 198, 199). The IM-MS three-dimensional Driftscope plot, which correlates the *m/z* of ions with their arrival time distribution, further confirmed the oligomeric states of these IAPP analogues. The I26P-

hIAPP variant had the least signal from higher-order assemblies and existed predominantly in a monomeric form, consistent with its lower aggregation propensity. Notably, the S20G variant has a lower oligomer intensity compared to others, even though it aggregates faster, but this is more likely due to the rapid transition of the higher-order oligomers into fibrils, which were not detected by IM-MS.

IM-MS further identified hetero-oligomer formation in the 1:1 molar ratio pairwise mixture of the IAPP peptides. The samples exhibited both homo- and hetero-oligomers. The ATDs of WT-homodimer, H18L-homodimer, and WT-H18L-heterodimers were found to populate a dominant conformer with a drift time of approximately 4.5 ms, along with a minor amount of more compact species at around 2.5 ms (Fig 11). It was reported that the relative intensity of this compact species in WT-H18L-IAPP-heterodimers is greater than that in H18L-IAPP-homodimer, but lower than that in WT-homodimers suggesting a compromise in structural adaptation in hetero-oligomers. Young *et al.* proposed that the greater relative proportion of the more expanded conformers correlates with faster amyloid formation, which is consistent with the shorter fibrillation lag times of H18L-IAPP and the H18L-hIAPP mixture as detected by ThT fluorescence (198). This hypothesis was further supported by the observation of the H18L-WT heterotrimer and H18L-IAPP homotrimer which were observed with a second species with an arrival time of ~8.6 ms, suggesting a more extended conformer. The WT-homotrimer, on the other hand, was observed with only one detectable species with an arrival time ~7.0 ms, corresponding to a more compact conformation (198). I26P, although reported not to homo-oligomerise in isolation, was observed to form hetero-dimers in the presence of WT-IAPP. The conformation of the I26P-WT heterodimer is indistinguishable from that of WT-homodimers based on their ATDs (198). These IM-MS observations highlight the influence of co-polymerisation on changing the aggregation propensity, indicating that peptides with more amyloidogenic sequences tend to dominate the amyloidogenic pathway. ThT fluorescence assays, demonstrated that the lag time for each peptide mixture was dominated by the lag time of the fastest aggregating sequence (Fig 12 a–f(i)). For instance, the mixture of H18L-IAPP with the faster aggregating S2G peptide resulted in ThT positive aggregates immediately, exhibiting a lag-time shorter than H18L alone. Additionally, the absence of biphasic kinetics in the ThT assays strongly suggested co-assembly between IAPP variants, rather than independent aggregation during the early stages (Fig 12 a–f(i)). The concept of conformation templating posits that the structural characteristics of highly amyloid-forming species can be imposed onto less amyloidogenic counterparts. This may explain the observation in the IM-MS data, which reveals an increase in both the population and intensity of these structurally expanded species, which related to the rate of amyloid formation (200–202). However, the effect of peptide mixtures on the lag phase of assembly cannot be simply explained by the cross-seeding (198). ThT fluorescence profiles indicate that WT fibrils are only able to seed fibril formation of the same peptide sequence (WT monomer), and the same specificity is observed with S20G fibrils as seeds. Collectively, solution kinetic studies of sequence variants and the use of ESI-IMS-MS for the detection, quantification, and profiling of transient species offer a robust approach to investigate the early stages of amyloid assembly.

IM-MS can also be used as a sensitive tool for characterising the co-assembly of the amyloid proteins from different systems. For instance, IM-MS has detected the co-aggregation of

human R3-tau, which is involved in Alzheimer's disease (AD), with hIAPP. The mass spectrum and injection energy studies revealed the R3-IAPP hetero-oligomer with peaks at n/z = (1 + 1)/+5, (1 + 1)/+7, corresponding to the 1:1 hetero-oligomers of R3 and IAPP, where n is the oligomer number and z is the charge (203, 204) The hetero dimers, tetramers and hexamers were reported from the ATDs (Fig 13). The observation from IM-MS suggested a potential catalytic role of the R3-IAPP mixture in the R3 aggregation, highlighting the complex interplay between IAPP and other amyloid-forming systems. This experiment also showcases the utility of IM-MS in clinical diagnostics and patient profiling, particularly its capacity to identify and characterise the hetero-oligomers formed by hIAPP and other amyloid-forming proteins that could potentially aggravate disease symptoms. Moreover, the influence of hIAPP, Aβ or tau protein co-assembly on fibrillation kinetics and toxicity necessitates additional research. IM-MS has also been used to study co-oligomers of IAPP and Aβ (205).

3.5 Applications of IM-MS in the study of inhibitors of hIAPP aggregation and toxicity

Amyloidogenic proteins are implicated in multiple human disorders, such as Alzheimer's disease and T2DM. Many treatments have failed in clinical trials as their administration is past the point of irreparable damage (206). Thus, researchers have long been searching for potential compounds capable of disrupting protein aggregation. The search for therapeutic agents for hIAPP aggregation deceleration and inhibition is crucial for anti-amyloid treatments and may also shed light on aggregation and toxicity mechanisms. IM-MS can be used to rapidly detect small molecules that bind to the amyloidogenic proteins, elucidate the binding modes and stoichiometry, and monitor the structural changes under the binding event. This makes IM-MS an invaluable technique in the field of drug discovery.

Young *et al.* have showcased an IM-MS-based high-throughput method to identify interactions between small molecule candidates and hIAPP and categorise the inhibition mechanism (199). Ten compounds were selected as test cases based on their known effect of hIAPP aggregation, including Fast Green FCF (FG), Epigallocatechin gallate (EGCG) and silibinin together with 1*H*-B-SA and ibuprofen. These molecules were mixed with hIAPP, and their gas-phase behaviour was monitored using IM-MS. The ESI mass spectrum indicates that FG binds to the +2 and +3 charge states of hIAPP monomers (these monomer charge states populate at least two conformers, a compact conformer and a more amyloid-prone extended conformer) and the +4 dimeric. This binding mode, where the small molecules bind to the hIAPP with specific n^{z+} (where n is the oligomeric state and z is the charge state) and conformation, were classified as specific binding events (199). The mass spectrum demonstrated that the presence of FG alters the distribution of +3 monomer ions, and the population of more compacted conformers of hIAPP differed compared to those observed in the absence of FG. The IM-MS Driftscope plot showed no higher-order oligomer species but only the monomeric hIAPP-FG complex, supporting the mode of inhibition by FG being specific. Further evidence from tandem MS experiments showed that such specific binding has a higher gas-phase stability than their non-specific binding counterparts, and the ATD revealed that the more compact monomeric-hIAPP species formed as the result of specific binding.

In contrast, the non-specific binding of 1*H*-B-SA and/or lack of inhibition by ibuprofen and three other compounds were also clearly characterised by ESI-IMS-MS. The mass spectrum and ESI-IM-MS Driftscope plots of 1*H*-B-SA with hIAPP reveal a series of ions with multiple ligands (up to seven ligands) bound to each monomeric conformer. This type of binding can be classified as non-specific. The ability of ESI-IM-MS to distinguish between specific and non-specific binding is an important feature. The compounds ibuprofen, aspirin, benzimidazole and hemin, when mixed with hIAPP, showed no changes in the hIAPP monomeric charge state distribution or the oligomer formation in ESI-IM-MS. TEM further confirmed the fibrillation of hIAPP. Collectively, the results indicate the lack of inhibition these small molecules have in hIAPP amyloid formation. In addition, the colloidal binding mode, where multiple small molecules aggregate into a larger complex, was observed for Congo red (CR). The mass spectrum and the Driftscope plot show a large population of higher-order species resulting from the CR self-assembly. Monomeric species, however, were still observed, but there was little hIAPP oligomer signal intensity. This is presumably due to the low intensities compared with those of CR aggregates, or they were indeed absent as a result of small molecule binding. This is an important observation since small molecules which self-aggregate can lead to promiscuous non-specific inhibitors. The ESI-IM-MS analysis and resulting Driftscope plots for each candidate small molecule served as a binding fingerprint that represent different types of binding modes. These include specific, colloidal, non-specific, and lack of inhibition, illustrating the straightforward characterisation and differentiation of the spectral fingerprints and their potential for future drug screening efforts.

A further application of this method involved screening a further 30 candidate compounds in a 96-well plate format. The use of a plate based format holds the promise for significantly improving the efficiency of the discovery of inhibitors of hIAPP amyloid assembly. Starting from the screen of a library of novel molecules that have similar structures to those of the previously reported inhibitors, one emerged as a new inhibitor of hIAPP aggregation, while three others showed nonspecific binding to hIAPP; the rest showed lack of inhibition. The successful compound, identified as compound 26, was a structural analogue of chloronaphthoquinine–tryptophan. At higher concentrations, compound 26 was specifically bound to the hIAPP monomer, preventing fibril formation and leading to the formation of amorphous aggregates. Fragmentation techniques coupled with this IM-MS screening method offer another dimension for the study of binding affinity (155, 207). This work broadens the application of the ESI-IM-MS screening technique to additional amyloid systems, including Aβ. Their work resulted in identifying new inhibitors of Aβ40 (208).

4. Advances and tandem MS/IM-MS

As illustrated in the above studies, IM-MS offers unique insights into the structure and dynamics of IAPP. Recent advances in IM-MS instrumentation have resulted in enhanced sensitivity, resolution, and the capability to perform tandem ion mobility experiments (116). Tandem IM allows multiple rounds of selection of particular conformational species (116). Tandem IM can be “tandem-in-space” where the selections of ion and activation occur in different regions of the instruments, or “tandem-in-time” where the ions are first accumulated and then activated in the space region (116). Since the pioneering

work by the Smith group demonstrating the use of tandem DTIMS devices in enhancing peptide fragmentation coverage, different types of IM have been combined with tandem IM. This includes combining FAIMS with DTIMS, which leads to enhanced sensitivity in conformational state detections (209–211). The Clemmer group pioneered the use of tandem IM for the study of native proteins, demonstrating its efficiency and sensitivity in studies of detailed ubiquitin conformational families (209, 210). In 2017, the Bleiholder group reported a tandem trapped ion mobility spectrometry (TIMS-TIMS) analyser (212). The system features two dimensionally identical TIMS units connected via an interface with two apertures, facilitating ion gating through electric potential modulation at these apertures. A transmitting DC voltage applied at the second aperture selectively allows mobility-separated ions from the first TIMS (TIMS-1) to pass to the second TIMS (TIMS-2). This enhances ion mobility-selection of analytes. In the interface region, ions can undergo collisional activation or dissociation, followed by direct mass detection or a second mobility separation in TIMS-2. This tandem ion-mobility separation approach, combined with activation techniques, significantly improves sequence coverage and correlates ion kinetics and energetics to structural changes (212).

Another significant milestone in the field was the release of the commercialised cyclic TWIMS IM-MS instrument (cIM-MS) that improved both the ion mobility resolution and conformer isolation significantly (213). The cyclic ion mobility (cIM) device consists of a 98 cm path length orthogonally to the main ion optical axis, allowing multipass separation for the enhanced resolution (approximately 750 after 100 passes) and tandem IM/IM experiments (213). The Thalassinos group were the first to show that cIM-MS is applicable to studying the native gas phase stability and unfolding using protein standards, including cytochrome C and concanavalin (125, 136). cIM has also been recently applied to demonstrate the dissociation and aggregation of jack bean urease under a temperature-controlled nano-electrospray ionisation source, demonstrating the usability of advanced cIM in studying protein aggregation in real-time (214). A tandem IM-MS method for detailed characterisation of protein unfolding pathways termed “slice-CA” with multiple rounds of IM-separation and activation was developed, aiding the understanding of the energetics of protein gas-phase behaviour (136). Another important development in this field is that of structures for lossless ion manipulation (SLIM) and an analogous with serpentine ultralong path with extended routing (SUPER) SLIM and multilevel SLIM (215–218). These SLIM techniques could provide ultrahigh-resolution mobility separation (R~1860) of the protein conformations and help avoid the data collected from “roll-over” in multi-pass analysis, whereby the high-mobility ions overlap with the lower-mobility species (116).

The first application of tandem IM-MS (IM^2, where the number represents the rounds of IM selection) to study IAPP was recently published by Eldrid *et al.* Tandem IM-MS (cyclic IM-MS) separated the +4 hIAPP dimers into early and later slices of 2 ms, which were then injected in the prestore array and re-injected into the cIM device for further mobility analysis at incremented voltages. This method is termed “Slice-CA” (136). The Slice-CA ATDs of both slices were superimposed, demonstrating the interconversion of dimeric conformations after activation. The Slice-CA method provides exceptional promise for understanding the structural conversion and dynamics of hIAPP. The tandem IM-MS approach developed by Eldrid *et al.* may open a new avenue for linking the relationship between structural dynamics

and the toxicity and amyloidogenicity of not only hIAPP, but also as a fundamental strategy for studying other amyloid-forming proteins. In future applications IM^n could be used to select specific conformational subpopulations, measure the comparative differences in stability induced by ligand binding and elucidate even more detailed structural behaviours of gas-phase proteins during activation at a higher resolution.

We can also expect that future, tandem IM techniques and native top-down MS workflow can be optimised to study hIAPP amyloid assembly at ultrahigh resolution. Tandem IM coupled with electron-capture dissociation can provide another dimension for the study of protein-protein interactions, protein-ligand interactions and ligand binding states. These can offer structural and mechanistic insight into the hIAPP initial oligomerisation and study the effect of hIAPP-small molecule interactions. As tandem IM becomes more readily accessible, we anticipate that tandem IM will play a pivotal role in advancing the study of structural dynamics and opening new frontiers in this field.

5. Conclusions and Future Directions

In this review, we emphasise the significance of understanding hIAPP amyloidogenicity and cytotoxicity via a structural perspective, particularly using IM-MS to reveal transient, lowly-populated, and toxic oligomers populated early in the aggregation pathway (38, 60, 73, 74). IM-MS extensively explored the intrinsic amyloidogenicity and toxicity that may be present within the hIAPP sequence, such as the disulphide bond, specific amyloidogenic domains, and the key S28P substitution (30, 96, 154, 155). IM-MS also measures hIAPP structural dynamics and changes in amyloid formation under the influence of Cu^{2+} and Zn^{2+} binding (184, 188). Additionally, IM-MS is valuable for delineating the types of aggregates present in patient-derived tissue samples and detecting the co-assembly of hIAPP with other IAPP variants and various amyloid-forming proteins, such as tau and Aβ (198, 204). This capability is crucial in devising preventive strategies for clinical intervention and monitoring disease progression associated with these protein assemblies. Furthermore, IM-MS enables high-throughput screening for amyloidogenic protein inhibitors and identifies their interaction modes (199). Thus, the IM-MS approach could also act as the pre-selection tool for hIAPP species and the potential inhibitors for further structural dynamics studies and optimise the structural-based drug design for hIAPP-induced cytotoxicity.

IM-MS has demonstrated its uniqueness in characterising transient hIAPP oligomers, but a few limitations of this approach and future expectations need to be mentioned. ESI-IM-MS measures hIAPP in the gas phase, and this can result in some hydrophobic interactions not being captured which may cause deviations in the hIAPP conformation and interactions compared to those in the solution phase (219, 220). Thus, translating gas-phase observations of hIAPP to *in vivo* behaviour necessitates supplementary experiments using other biophysical techniques. Another limitation for many current IM-MS instrumentation is both the mass and ion mobility resolving power. The lack of isotopic resolution can result in incorrect assignment of peaks as being due to compact/extended conformers rather than overlapping monomer/dimer species, while the lack of ion mobility resolution is not able to differentiate between co-existing conformers sensitively. As reported by Ridgway *et al.*, no significant differences were found in the CCS distributions among the IAPP variants,

arguably due to the low-resolving power (30). Furthermore, the initial peak assignment of IAPP variants at m/z = 1950 (Fig 9) as monomeric 1^{2+} ions was recently revised to be a mixture of 1^{2+} and 2^{4+} (Fig 6 (C)), rather than pure monomeric species (30, 136). These examples underscore the resolution constraints of current IM-MS technology and emphasise the pressing need for more advanced, higher resolution tandem IM techniques such as cIM-MS and SLIMS techniques and native top-down methods to achieve unprecedented resolution in characterising elusive structures. We expect the integration of advanced IM-MS techniques and future endeavours to bridge the gap between hIAPP *in vitro* IM-MS experiments and *in vivo* biological relevance, linking not only the hIAPP structural dynamics and cellular cytotoxicity but also opening avenues for the development of novel therapeutic strategies against hIAPP induced T2DM and even other amyloid diseases.

Acknowledgements

ZD is supported by the MRC iCASE PhD studentship (MR/W006774/1). This work was supported by the Wellcome Trust 209250/Z/ 17/Z and 107927/Z/15/Z and a grant from the USPHS NIH R01GM078114

Abbreviations

AD	Alzheimer’s disease
Aβ	Amyloid beta
ATD	Arrival time distribution
AFM	Atomic force microscopy
CD	Circular dichroism
CA	Collision activation
CCS	Collision cross section
CID	Collision induced dissociation
CIU	Collision induced unfolding
CR	Congo red
Cryo-EM	Cryogenic electron miscroscopy
cIM	Cyclic ion mobility
DMA	Differential mobility analysis
DTIMS	Drift-tube ion mobility spectrometry
EPR	Electron paramagnetic resonance
ESI	Electrospray ionisation
ER	Endoplasmic reticulum
EGCG	Epigallocatechin gallate

FG	Fast Green FCF
FRET	Fluorescence energy transfer
FAIMS	High field asymmetric waveform ion mobility spectrometry
hIAPP	Human islet amyloid polypeptide
IR	Infrared
IM	Ion-Mobility
IM-MS	Ion-mobility Mass Spectrometry
LAESI	Laser ablation electrospray ionization
MS	Mass Spectrometry
m/z	Mass-to-charge ratio
MD	Molecular dynamics
nESI	Nano-electrospray ionisation
NMR	Nuclear magnetic resonance
PTM	Post-translational modification
qToF	Quadrupole Time-of-Flight
rIAPP	Rat iselt amyloid polypeptide
SDS	Sodium dodecyl sulfate
ThT	Thioflavin T
ToF	Time-of-Flight
TIMS	Trapped ion-mobility spectrometry
TWIMS	Travelling-wave ion-mobility mass spectrometry
2D-IR	two-dimensional infrared spectroscopy
T2DM	Type II diabetes Mellitus
T2D	Type-2 Diabetes
WT	Wild type

References

1. Kahn SE, D'Alessio DA, Schwartz MW, Fujimoto WY, Ensinck JW, Taborsky GJ, and Porte D. 1990. Evidence of cosecretion of islet amyloid polypeptide and insulin by β-cells. Nestle. Nutr. Works. Se. 39:634–638.

2. Lukinius A, Wilander E, Westermark GT, Engström U, and Westermark P. 1989. Co-localization of islet amyloid polypeptide and insulin in the B cell secretory granules of the human pancreatic islets. Diabetologia. 32:240–244. [PubMed: 2668077]

3. Stridsberg M, Sandler S, and Wilander E. 1993. Cosecretion of islet amylid polypeptide (IAPP) and insulin from isolated rat pancreatic islets following stimulation or inhibition of β-cell function. Regul. Pept. 45:363–70. [PubMed: 8351401]

4. Lutz TA. 2013. The interaction of amylin with other hormones in the control of eating. Diabetes, Obesity and Metabolism. 15:99–111.

5. Lutz TA. 2010. The role of amylin in the control of energy homeostasis. American Journal of Physiology - Regulatory Integrative and Comparative Physiology. 298:R1475–R1484. [PubMed: 20357016]

6. Lutz TA. 2012. Control of energy homeostasis by amylin. Cellular and Molecular Life Sciences. 69:1947–1965. [PubMed: 22193913]

7. Potter KJ, Abedini A, Marek P, Klimek AM, Butterworth S, Driscoll M, Baker R, Nilsson MR, Warnock GL, Oberholzer J, Bertera S, Trucco M, Korbutt GS, Fraser PE, Raleigh DP, and Verchere CB. 2010. Islet amyloid deposition limits the viability of human islet grafts but not porcine islet grafts. Proc. Natl. Acad. Sci. 107:4305–4310. [PubMed: 20160085]

8. Udayasankar J, Kodama K, Hull RL, Zraika S, Aston-Mourney K, Subramanian SL, Tong J, Faulenbach MV, Vidal J, and Kahn SE. 2009. Amyloid formation results in recurrence of hyperglycaemia following transplantation of human IAPP transgenic mouse islets. Diabetologia. 52:145–153. [PubMed: 19002432]

9. Wang J, Xu J, Finnerty J, Furuta M, Steiner DF, and Verchere CB. 2001. The prohormone convertase enzyme 2 (PC2) is essential for processing pro-islet amyloid polypeptide at the NH2-terminal cleavage site. Nestle. Nutr. Works. Se. 50:534–539.

10. Badman MK, Shennan KIJ, Jermany JL, Docherty K, and Clark A. 1996. Processing of pro-islet amyloid polypeptide (proIAPP) by the prohormone convertase PC2. FEBS Lett. 378:227–231. [PubMed: 8557106]

11. Higham CE, Jaikaran ETAS, Fraser PE, Gross M, and Clark A. 2000. Preparation of synthetic human islet amyloid polypeptide (IAPP) in a stable conformation to enable study of conversion to amyloid-like fibrils. FEBS Lett. 470:55–60. [PubMed: 10722845]

12. Sanke T, Bell GI, Sample C, Rubenstein AH, and Steiner DF. 1988. An islet amyloid peptide is derived from an 89-amino acid precursor by proteolytic processing. J. Biol. Chem. 263:17243–6. [PubMed: 3053705]

13. Marzban L, Soukhatcheva G, and Bruce Verchere C. 2005. Role of carboxypeptidase E in processing of pro-islet amyloid polypeptide in β-cells. Endocrinology. 146:1808–17. [PubMed: 15618358]

14. Bower RL, Yule L, Rees TA, Deganutti G, Hendrikse ER, Harris PWR, Kowalczyk R, Ridgway Z, Wong AG, Swierkula K, Raleigh DP, Pioszak AA, Brimble MA, Reynolds CA, Walker CS, and Hay DL. 2018. Molecular signature for receptor engagement in the metabolic peptide hormone amylin. ACS Pharmacol. Transl. Sci. 1:32–49. [PubMed: 32219203]

15. Paulsson JF and Westermark GT. 2005. Aberrant processing of human proislet amyloid polypeptide results in increased amyloid formation. Nestle. Nutr. Works. Se. 54:2117–2125.

16. Williamson JA and Miranker AD. 2007. Direct detection of transient α-helical states in islet amyloid polypeptide. Protein Sci. 16:110–117. [PubMed: 17123962]

17. Wiltzius JJW, Sievers SA, Sawaya MR, and Eisenberg D. 2009. Atomic structures of IAPP (amylin) fusions suggest a mechanism for fibrillation and the role of insulin in the process. Protein Sci. 18:1521–1530. [PubMed: 19475663]

18. Camargo DCR, Tripsianes K, Buday K, Franko A, Göbl C, Hartlmüller C, Sarkar R, Aichler M, Mettenleiter G, Schulz M, Böddrich A, Erck C, Martens H, Walch AK, Madl T, Wanker EE, Conrad M, Hrabě de Angelis M, and Reif B. 2017. The redox environment triggers conformational changes and aggregation of hIAPP in type II diabetes. Sci. Rep. 7:44041. [PubMed: 28287098]

19. Raleigh D, Zhang X, Hastoy B, and Clark A. 2017. The β-cell assassin: IAPP cytotoxicity. J. Mol. Endocrinol. 59:R121–R140. [PubMed: 28811318]

20. Abedini A and Raleigh DP. 2009. A role for helical intermediates in amyloid formation by natively unfolded polypeptides? Phys. Biol. 6:15005.
21. Blanchard BJ, Chen A, Rozeboom LM, Stafford KA, Weigele P, and Ingram VM. 2004. Efficient reversal of alzheimer's disease fibril formation and elimination of neurotoxicity by a small molecule. PNAS. 101:14326–14332. [PubMed: 15388848]
22. Porat Y, Abramowitz A, and Gazit E. 2006. Inhibition of amyloid fibril formation by polyphenols: structural similarity and aromatic interactions as a common inhibition mechanism. Chemical Biology and Drug Design. 67:27–37. [PubMed: 16492146]
23. Westermark P, Engström U, Johnson KH, Westermark GT, and Betsholtz C. 1990. Islet amyloid polypeptide: pinpointing amino acid residues linked to amyloid fibril formation. Proc. Natl. Acad. Sci. 87:5036–5040. [PubMed: 2195544]
24. Ashburn TT and Lansbury PT. 1993. Interspecies sequence variations affect the kinetics and thermodynamics of amyloid formation: peptide models of pancreatic amyloid. J. Am. Chem. Soc. 115:11012–11013.
25. Abedini A and Raleigh DP. 2006. Destabilization of human IAPP amyloid fibrils by proline mutations outside of the putative amyloidogenic domain: is there a critical amyloidogenic domain in human IAPP? J. Mol. Biol. 355:274–281. [PubMed: 16303136]
26. Koo BW, Hebda JA, and Miranker AD. 2008. Amide inequivalence in the fibrillar assembly of islet amyloid polypeptide. Protein Eng. Des. Sel. 21:147–154. [PubMed: 18299291]
27. Green J, Goldsbury C, Mini T, Sunderji S, Frey P, Kistler J, Cooper G, and Aebi U. 2003. Full-length rat amylin forms fibrils following substitution of single residues from human amylin. J. Mol. Biol. 326:1147–1156. [PubMed: 12589759]
28. Noh D, Bower RL, Hay DL, Zhyvoloup A, and Raleigh DP. 2020. Analysis of amylin consensus sequences suggests that human amylin is not optimized to minimize amyloid formation and provides clues to factors that modulate amyloidogenicity. ACS Chem. Biol. 15:1408–1416. [PubMed: 32364695]
29. Khemtemourian L, Guillemain G, Foufelle F, and Killian JA. 2017. Residue specific effects of human islet polypeptide amyloid on self-assembly and on cell toxicity. Biochimie. 142:22–30. [PubMed: 28778718]
30. Ridgway Z, Eldrid C, Zhyvoloup A, Ben-Younis A, Noh D, Thalassinos K, and Raleigh DP. 2020. Analysis of proline substitutions reveals the plasticity and sequence sensitivity of human IAPP amyloidogenicity and toxicity. Biochemistry-us. 59:742–754.
31. Sakagashira S, Sanke T, Hanabusa T, Shimomura H, Ohagi S, Kumagaye KY, Nakajima K, and Nanjo K. 1996. Missense mutation of amylin gene (S20G) in japanese NIDDM patients. Nestle. Nutr. Works. Se. 45:1279–1281.
32. Lee SC, Hashim Y, Li JKY, Ko GTC, Critchley JAJH, Cockram CS, and Chan JCN. 2001. The islet amyloid polypeptide (amylin) gene S20G mutation in chinese subjects: evidence for associations with type 2 diabetes and cholesterol levels. Clin. Endocrinol. 54:541–546.
33. Sakagashira S, Hiddinga HJ, Tateishi K, Sanke T, Hanabusa T, Nanjo K, and Eberhardt NL. 2000. S20G mutant amylin exhibits increased in vitro amyloidogenicity and increased intracellular cytotoxicity compared to wild-type amylin. Am. J. Pathol. 157:2101–2109. [PubMed: 11106582]
34. Ma Z, Westermark GT, Sakagashira S, Sanke T, Gustavsson Å, Sakamoto H, Engström U, Nanjo K, and Westermark P. 2001. Enhanced in vitro production of amyloid-like fibrils from mutant (s20g) islet amyloid polypeptide. Amyloid. 8:242–249. [PubMed: 11791616]
35. Cao P, Tu L, Abedini A, Levsh O, Akter R, Patsalo V, Schmidt AM, and Raleigh DP. 2012. Sensitivity of amyloid formation by human islet amyloid polypeptide to mutations at residue 20. J. Mol. Biol. 421:282–295. [PubMed: 22206987]
36. Krotee P, Rodriguez JA, Sawaya MR, Cascio D, Reyes FE, Shi D, Hattne J, Nannenga BL, Oskarsson ME, Philipp S, Griner S, Jiang L, Glabe CG, Westermark GT, Gonen T, and Eisenberg DS. 2017. Atomic structures of fibrillar segments of hIAPP suggest tightly mated β-sheets are important for cytotoxicity. eLife. 6:e19273. [PubMed: 28045370]
37. Xu Y, Maya-Martinez R, Guthertz N, Heath GR, Manfield IW, Breeze AL, Sobott F, Foster R, and Radford SE. 2022. Tuning the rate of aggregation of hIAPP into amyloid using small-molecule modulators of assembly. Nat. Commun. 13:1040. [PubMed: 35210421]

38. Abedini A, Plesner A, Cao P, Ridgway Z, Zhang J, Tu L, Middleton CT, Chao B, Sartori DJ, Meng F, Wang H, Wong AG, Zanni MT, Verchere CB, Raleigh DP, and Schmidt AM. 2016. Time-resolved studies define the nature of toxic IAPP intermediates, providing insight for anti-amyloidosis therapeutics. eLife. 5:e12977. [PubMed: 27213520]
39. Edelman SV and Weyer C. 2002. Unresolved challenges with insulin therapy in type 1 and type 2 diabetes: potential benefit of replacing amylin, a second β-cell hormone. Diabetes Technology & Therapeutics. 4:175–189. [PubMed: 12079621]
40. Kruger DF, Gatcomb PM, and Owen SK. 1999. Clinical implications of amylin and amylin deficiency. Diabetes Educ. 25:389–397. [PubMed: 10531859]
41. Jaikaran ETAS and Clark A. 2001. Islet amyloid and type 2 diabetes: from molecular misfolding to islet pathophysiology. Biochimica et Biophysica Acta - Molecular Basis of Disease. 1537:179–203.
42. Hull RL, Westermark GT, Westermark P, and Kahn SE. 2004. Islet amyloid: a critical entity in the pathogenesis of type 2 diabetes. J. Clin. Endocrinol. Metab. 89:3629–3643. [PubMed: 15292279]
43. Hutton JC. 1982. The internal pH and membrane potential of the insulin-secretory granule. Biochem. J. 204:171–178. [PubMed: 6126183]
44. Janciauskiene S, Eriksson S, Carlemalm E, and Ahrén B. 1997. B cell granule peptides affect human islet amyloid polypeptide (IAPP) fibril formation in vitro. Biochem. Biophys. Res. Commun. 236:580–585. [PubMed: 9245692]
45. JAIKARAN ETAS, NILSSON MR, and CLARK A. 2004. Pancreatic beta-cell granule peptides form heteromolecular complexes which inhibit islet amyloid polypeptide fibril formation. Biochem. J. 377:709–716. [PubMed: 14565847]
46. Westermark P, Li ZC, Westermark GT, Leckström A, and Steiner DF. 1996. Effects of beta cell granule components on human islet amyloid polypeptide fibril formation. FEBS Lett. 379:203–206. [PubMed: 8603689]
47. Knight JD, Williamson JA, and Miranker AD. 2008. Interaction of membrane-bound islet amyloid polypeptide with soluble and crystalline insulin. Protein Sci. 17:1850–1856. [PubMed: 18765820]
48. Nedumpully-Govindan P, Yang Y, Andorfer R, Cao W, and Ding F. 2015. Promotion or inhibition of islet amyloid polypeptide aggregation by zinc coordination depends on its relative concentration. Biochemistry-us. 54:7335–7344.
49. Höppener JWM, Ahrén B, and Lips CJM. 2000. Islet amyloid and type 2 diabetes mellitus. N. Engl. J. Med. 343:411–419. [PubMed: 10933741]
50. Westermark P. 1972. Quantitative studies of amyloid in the islets of langerhans. Upsala J. Med. Sci. 77:91–94. [PubMed: 4116019]
51. Zraika S, Hull RL, Udayasankar J, Aston-Mourney K, Subramanian SL, Kisilevsky R, Szarek WA, and Kahn SE. 2009. Oxidative stress is induced by islet amyloid formation and time-dependently mediates amyloid-induced beta cell apoptosis. Diabetologia. 52:626–635. [PubMed: 19148619]
52. Dunne A, Subramanian SL, Hull RL, Tannahill GM, Sharp FA, Becker C, Franchi L, Yoshihara E, Chen Z, Mullooly N, Mielke LA, Harris J, Coll RC, Mills KHG, Mok KH, Newsholme P, Nuñez G, Yodoi J, Kahn SE, Lavelle EC, and O'Neill LAJ. 2010. Activation of the NLRP3 inflammasome by islet amyloid polypeptide provides a mechanism for enhanced IL-1β 2 in type 2 diabetes. Nat. Immunol. 11:897–904. [PubMed: 20835230]
53. Casas S, Gomis R, Gribble FM, Altirriba J, Knuutila S, and Novials A. 2007. Impairment of the ubiquitin-proteasome pathway is a downstream endoplasmic reticulum stress response induced by extracellular human islet amyloid polypeptide and contributes to pancreatic β-cell apoptosis. Nestle. Nutr. Works. Se. 56:2284–2294.
54. Subramanian SL, l Hull R, Zraika S, Aston-Mourney K, Udayasankar J, and Kahn SE. 2012. CJUN N-terminal kinase (JNK) activation mediates islet amyloid-induced beta cell apoptosis in cultured human islet amyloid polypeptide transgenic mouse islets. Diabetologia. 55:166–174. [PubMed: 22038516]
55. Park YJ, Lee S, Kieffer TJ, Warnock GL, Safikhan N, Speck M, Hao Z, Woo M, and Marzban L. 2012. Deletion of fas protects islet beta cells from cytotoxic effects of human islet amyloid polypeptide. Diabetologia. 55:1035–1047.

56. Zhang S, Liu J, Dragunow M, and Cooper GJS. 2003. Fibrillogenic amylin evokes islet β-cell apoptosis through linked activation of a caspase cascade and JNK1. J. Biol. Chem. 278:52810–52819. [PubMed: 14532296]
57. Westwell-Roper C, Dai DL, Soukhatcheva G, Potter KJ, van Rooijen N, Ehses JA, and Verchere CB. 2011. IL-1 blockade attenuates islet amyloid polypeptide-induced proinflammatory cytokine release and pancreatic islet graft dysfunction. J. Immunol. 187:2755–2765. [PubMed: 21813778]
58. Abedini A, Cao P, Plesner A, Zhang J, He M, Derk J, Patil SA, Rosario R, Lonier J, Song F, Koh H, Huilin Li, Raleigh DP, and Schmidt AM. 2018. RAGE binds preamyloid IAPP intermediates and mediates pancreatic β cell proteotoxicity. J. Clin. Invest. 128:682–698. [PubMed: 29337308]
59. Ashcroft FM and Rorsman P. 2012. Diabetes mellitus and the β cell: the last ten years. Cell. 148:1160–1171. [PubMed: 22424227]
60. Lam YPY, Wootton CA, Hands-Portman I, Wei J, Chiu CKC, Romero-Canelon I, Lermyte F, Barrow MP, and O'Connor PB. 2020. Determination of the aggregate binding site of amyloid protofibrils using electron capture dissociation tandem mass spectrometry. J. Am. Soc. Mass Spectrom. 31:267–276. [PubMed: 31922736]
61. Ferrone F. 1999. Analysis of protein aggregation kinetics. Methods Enzymol. 309:256–274. [PubMed: 10507029]
62. Glabe CG. 2006. Common mechanisms of amyloid oligomer pathogenesis in degenerative disease. Neurobiology of Aging. 27:570–575. [PubMed: 16481071]
63. Pithadia A, Brender JR, Fierke CA, and Ramamoorthy A. 2016. Inhibition of IAPP aggregation and toxicity by natural products and derivatives. Journal of Diabetes Research. 2016:2046327. [PubMed: 26649317]
64. Ruschak AM and Miranker AD. 2007. Fiber-dependent amyloid formation as catalysis of an existing reaction pathway. Proc. Natl. Acad. Sci. 104:12341–12346. [PubMed: 17640888]
65. Camargo DCR, Chia S, Menzies J, Mannini B, Meisl G, Lundqvist M, Pohl C, Bernfur K, Lattanzi V, Habchi J, IA Cohen S, Knowles TPJ, Vendruscolo M, and Linse S. 2021. Surface-catalyzed secondary nucleation dominates the generation of toxic IAPP aggregates. Front. Mol. Biosci. 8:757425. [PubMed: 34790701]
66. Arosio P, Cukalevski R, Frohm B, Knowles TPJ, and Linse S. 2014. Quantification of the concentration of Aβ42 propagons during the lag phase by an amyloid chain reaction assay. J. Am. Chem. Soc. 136:219–225. [PubMed: 24313551]
67. Michaels TCT, Šarić A, Curk S, Bernfur K, Arosio P, Meisl G, Dear AJ, Cohen SIA, Dobson CM, Vendruscolo M, Linse S, and Knowles TPJ. 2020. Dynamics of oligomer populations formed during the aggregation of alzheimer's Aβ42 peptide. Nat. Chem. 12:445–451. [PubMed: 32284577]
68. Meisl G, Yang X, Hellstrand E, Frohm B, Kirkegaard JB, Cohen SIA, Dobson CM, Linse S, and Knowles TPJ. 2014. Differences in nucleation behavior underlie the contrasting aggregation kinetics of the Aβ40 and Aβ42 peptides. Proc. Natl. Acad. Sci. 111:9384–9389. [PubMed: 24938782]
69. Buell AK, Galvagnion C, Gaspar R, Sparr E, Vendruscolo M, Knowles TPJ, Linse S, and Dobson CM. 2014. Solution conditions determine the relative importance of nucleation and growth processes in α-synuclein aggregation. Proc. Natl. Acad. Sci. 111:7671–7676. [PubMed: 24817693]
70. Kayed R, Bernhagen J, Greenfield N, Sweimeh K, Brunner H, Voelter W, and Kapurniotu A. 1999. Conformational transitions of islet amyloid polypeptide (IAPP) in amyloid formation in vitro. J. Mol. Biol. 287:781–796. [PubMed: 10191146]
71. Glabe CG and Kayed R. 2006. Common structure and toxic function of amyloid oligomers implies a common mechanism of pathogenesis. In: Neurology. . pp. S74–S78.
72. Karamanos TK, Jackson MP, Calabrese AN, Goodchild SC, Cawood EE, Thompson GS, Kalverda AP, Hewitt EW, and Radford SE. 2019. Structural mapping of oligomeric intermediates in an amyloid assembly pathway. eLife. 8:e46574. [PubMed: 31552823]
73. Janson J, Ashley RH, Harrison D, McIntyre S, and Butler PC. 1999. The mechanism of islet amyloid polypeptide toxicity is membrane disruption by intermediate-sized toxic amyloid particles. Nestle. Nutr. Works. Se. 48:491–498.

74. Konarkowska B, Aitken JF, Kistler J, Zhang S, and Cooper GJS. 2006. The aggregation potential of human amylin determines its cytotoxicity towards islet β-cells. FEBS J. 273:3614–3624. [PubMed: 16884500]
75. Williamson JA, Loria JP, and Miranker AD. 2009. Helix stabilization precedes aqueous and bilayer-catalyzed fiber formation in islet amyloid polypeptide. J. Mol. Biol. 393:383–396. [PubMed: 19647750]
76. Goldsbury C, Goldie K, Pellaud J, Seelig J, Frey P, Müller SA, Kistler J, Cooper GJS, and Aebi U. 2000. Amyloid fibril formation from full-length and fragments of amylin. J. Struct. Biol. 130:352–362. [PubMed: 10940238]
77. Patil SM, Xu S, Sheftic SR, and Alexandrescu AT. 2009. Dynamic α-helix structure of micelle-bound human amylin. J. Biol. Chem. 284:11982–11991. [PubMed: 19244249]
78. Nanga RPR, Brender JR, Vivekanandan S, and Ramamoorthy A. 2011. Structure and membrane orientation of IAPP in its natively amidated form at physiological pH in a membrane environment. Biochim. Biophys. Acta (BBA) - Biomembr. 1808:2337–2342.
79. Apostolidou M, Jayasinghe SA, and Langen R. 2008. Structure of α-helical membrane-bound human islet amyloid polypeptide and its implications for membrane-mediated misfolding. J. Biol. Chem. 283:17205–17210. [PubMed: 18442979]
80. D Kirkitadze M, M Condron M, and Teplow DB. 2001. Identification and characterization of key kinetic intermediates in amyloid β-protein fibrillogenesis11Edited by F. Cohen. J. Mol. Biol. 312:1103–1119. [PubMed: 11580253]
81. Kessler JC, Rochet J, and Lansbury PT. 2003. The N-terminal repeat domain of α-synuclein inhibits β-sheet and amyloid fibril formation. Biochemistry-us. 42:672–678.
82. Maj M, Lomont JP, Rich KL, Alperstein AM, and Zanni MT. 2018. Site-specific detection of protein secondary structure using 2D IR dihedral indexing: a proposed assembly mechanism of oligomeric hIAPP. Chem. Sci. 9:463–474. [PubMed: 29619202]
83. Cao Q, Boyer DR, Sawaya MR, Ge P, and Eisenberg DS. 2020. Cryo-EM structure and inhibitor design of human IAPP (amylin) fibrils. Nat. Struct. Mol. Biol. 27:653–659. [PubMed: 32541896]
84. Sunde M and Blake C. 1997. The structure of amyloid fibrils by electron microscopy and x-ray diffraction. Advances in Protein Chemistry. 50:123–159. [PubMed: 9338080]
85. Cao Q, Boyer DR, Sawaya MR, Abskharon R, Saelices L, Nguyen BA, Lu J, Murray KA, Kandeel F, and Eisenberg DS. 2021. Cryo-EM structures of hIAPP fibrils seeded by patient-extracted fibrils reveal new polymorphs and conserved fibril cores. Nat. Struct. Mol. Biol. 28:724–730. [PubMed: 34518699]
86. Luca S, Yau W, Leapman R, and Tycko R. 2007. Peptide conformation and supramolecular organization in amylin fibrils: constraints from solid-state NMR. Biochemistry. 46:13505–13522. [PubMed: 17979302]
87. Sawaya MR, Sambashivan S, Nelson R, Ivanova MI, Sievers SA, Apostol MI, Thompson MJ, Balbirnie M, Wiltzius JJW, McFarlane HT, Ø Madsen A, Riekel C, and Eisenberg D. 2007. Atomic structures of amyloid cross-β spines reveal varied steric zippers. Nature. 447:453–457. [PubMed: 17468747]
88. Röder C, Kupreichyk T, Gremer L, Schäfer LU, Pothula KR, Ravelli RBG, Willbold D, Hoyer W, and Schröder GF. 2020. Cryo-EM structure of islet amyloid polypeptide fibrils reveals similarities with amyloid-β fibrils. Nat Struct Mol Biol. 27:660–667. [PubMed: 32541895]
89. Gallardo R, Iadanza MG, Xu Y, Heath GR, Foster R, Radford SE, and Ranson NA. 2020. Fibril structures of diabetes-related amylin variants reveal a basis for surface-templated assembly. Nat Struct Mol Biol. 27:1048–1056. [PubMed: 32929282]
90. Young L, Ndlovu H, Knapman TW, Harris SA, Radford SE, and Ashcroft AE. 2013. Monitoring oligomer formation from self-aggregating amylin peptides using ESI-IMS-MS. Int. J. Ion Mobility Spectrom. 16:29–39.
91. Woods LA, Radford SE, and Ashcroft AE. 2013. Advances in ion mobility spectrometry-mass spectrometry reveal key insights into amyloid assembly. Biochimica et Biophysica Acta - Proteins and Proteomics. 1834:1257–1268.
92. Yamashita M and Fenn JB. 1984. Electrospray ion source. Another variation on the free-jet theme. J. Phys. Chem. 88:4451–4459.

93. Karas M and Hillenkamp F. 1988. Laser desorption ionization of proteins with molecular masses exceeding 10,000 daltons. Anal. Chem. 60:2299–2301. [PubMed: 3239801]
94. Mann M, Meng CK, Wong SF, and Whitehouse CM. 1989. Electrospray ionization for mass spectrometry of large biomolecules. Sci. (N. Y. N.Y.). 246:64–71.
95. Britt HM, Cragnolini T, and Thalassinos K. 2022. Integration of mass spectrometry data for structural biology. Chemical Reviews. 122:7952–7986. [PubMed: 34506113]
96. Bleiholder C, Dupuis NF, Wyttenbach T, and Bowers MT. 2011. Ion mobility–mass spectrometry reveals a conformational conversion from random assembly to β-sheet in amyloid fibril formation. Nat. Chem. 3:172–177. [PubMed: 21258392]
97. Ruotolo BT, Benesch JLP, Sandercock AM, Hyung S, and Robinson CV. 2008. Ion mobility–mass spectrometry analysis of large protein complexes. Nat. Protoc. 3:1139–1152. [PubMed: 18600219]
98. Fenn LS, Kliman M, Mahsut A, Zhao SR, and McLean JA. 2009. Characterizing ion mobility-mass spectrometry conformation space for the analysis of complex biological samples. Anal. Bioanal. Chem. 394:235–244. [PubMed: 19247641]
99. Thalassinos K, Grabenauer M, Slade SE, Hilton GR, Bowers MT, and Scrivens JH. 2009. Characterization of phosphorylated peptides using traveling wave-based and drift cell ion mobility mass spectrometry. Anal. Chem. 81:248–254. [PubMed: 19117454]
100. Dodds JN and Baker ES. 2019. Ion mobility spectrometry: fundamental concepts, instrumentation, applications, and the road ahead. J. Am. Soc. Mass Spectrom. 30:2185–2195. [PubMed: 31493234]
101. Sivalingam GN, Cryar A, Williams MA, Gooptu B, and Thalassinos K. 2018. Deconvolution of ion mobility mass spectrometry arrival time distributions using a genetic algorithm approach: application to α1-antitrypsin peptide binding. Int. J. Mass Spectrom. 426:29–37.
102. Smith DP, Knapman TW, Campuzano I, Malham RW, Berryman JT, Radford SE, and Ashcroft AE. 2009. Deciphering drift time measurements from travelling wave ion mobility spectrometry-mass spectrometry studies. Eur. J. Mass Spectrom. 15:113–130.
103. France AP, Migas LG, Sinclair E, Bellina B, and Barran PE. 2020. Using collision cross section distributions to assess the distribution of collision cross section values. Anal. Chem. 92:4340–4348. [PubMed: 32053357]
104. Marchand A, Livet S, Rosu F, and Gabelica V. 2017. Drift tube ion mobility: how to reconstruct collision cross section distributions from arrival time distributions? Anal. Chem. 89:12674–12681. [PubMed: 29131943]
105. Marklund EG, Degiacomi MT, Robinson CV, Baldwin AJ, and Benesch JLP. 2015. Collision cross sections for structural proteomics. Structure. 23:791–799. [PubMed: 25800554]
106. Shelimov KB, Clemmer DE, Hudgins RR, and Jarrold MF. 1997. Protein structure in vacuo: gas-phase conformations of BPTI and cytochrome *c*. J. Am. Chem. Soc. 119:2240–2248.
107. Debaene F, Bœuf A, Wagner-Rousset E, Colas O, Ayoub D, Corvaïa N, Van Dorsselaer A, Beck A, and Cianférani S. 2014. Innovative native MS methodologies for antibody drug conjugate characterization: high resolution native MS and IM-MS for average DAR and DAR distribution assessment. Anal. Chem. 86:10674–10683. [PubMed: 25270580]
108. Christofi E and Barran P. 2023. Ion mobility mass spectrometry (IM-MS) for structural biology: insights gained by measuring mass, charge, and collision cross section. Chem. Rev. 123:2902–2949. [PubMed: 36827511]
109. Wang K, Qiu R, Zhang X, Gillig KJ, and Sun W. 2020. U-shaped mobility analyzer: a compact and high-resolution counter-flow ion mobility spectrometer. Anal. Chem. 92:8356–8363. [PubMed: 32391680]
110. Giles K, Pringle SD, Worthington KR, Little D, Wildgoose JL, and Bateman RH. 2004. Applications of a travelling wave-based radio-frequency-only stacked ring ion guide. Rapid Commun. Mass Spectrom. 18:2401–2414. [PubMed: 15386629]
111. Fernandez-Lima FA, Kaplan DA, and Park MA. 2011. Note: integration of trapped ion mobility spectrometry with mass spectrometry. Rev. Sci. Instrum. 82:126106. [PubMed: 22225261]
112. Revercomb HE and Mason EA. 1975. Theory of plasma chromatography/gaseous electrophoresis. Review. Anal. Chem. 47:970–983.

113. Giles K, Williams JP, and Campuzano I. 2011. Enhancements in travelling wave ion mobility resolution. Rapid Commun. Mass Spectrom. 25:1559–1566. [PubMed: 21594930]
114. Pringle SD, Giles K, Wildgoose JL, Williams JP, Slade SE, Thalassinos K, Bateman RH, Bowers MT, and Scrivens JH. 2007. An investigation of the mobility separation of some peptide and protein ions using a new hybrid quadrupole/travelling wave IMS/oa-ToF instrument. Int. J. Mass Spectrom. 261:1–12.
115. Bush MF, Hall Z, Giles K, Hoyes J, Robinson CV, and Ruotolo BT. 2010. Collision cross sections of proteins and their complexes: a calibration framework and database for gas-phase structural biology. Anal. Chem. 82:9557–9565. [PubMed: 20979392]
116. Eldrid C and Thalassinos K. 2020. Developments in tandem ion mobility mass spectrometry. Biochemical Society Transactions. 48:2457–2466. [PubMed: 33336686]
117. Reischl GP. 1991. Measurement of ambient aerosols by the differential mobility analyzer method: concepts and realization criteria for the size range between 2 and 500 nm. Aerosol Sci. Technol. 14:5–24.
118. Buryakov IA, Krylov EV, Nazarov EG, and Kh Rasulev U. 1993. A new method of separation of multi-atomic ions by mobility at atmospheric pressure using a high-frequency amplitude-asymmetric strong electric field. Int. J. Mass Spectrom. Ion Processes. 128:143–148.
119. Fernandez-Lima F, Kaplan DA, Suetering J, and Park MA. 2011. Gas-phase separation using a trapped ion mobility spectrometer. Int. J. Ion Mobility Spectrom. 14:93–98.
120. Seo J, Hoffmann W, Warnke S, Huang X, Gewinner S, Schöllkopf W, Bowers MT, von Helden G, and Pagel K. 2017. An infrared spectroscopy approach to follow β-sheet formation in peptide amyloid assemblies. Nat. Chem. 9:39–44. [PubMed: 27995915]
121. Khaled M, Rönnbäck I, Ilag LL, Gräslund A, Strodel B, and Österlund N. 2023. A hairpin motif in the amyloid-β peptide is important for formation of disease-related oligomers. J. Am. Chem. Soc. 145:18340–18354. [PubMed: 37555670]
122. Matthes D, Daebel V, Meyenberg K, Riedel D, Heim G, Diederichsen U, Lange A, and de Groot BL. 2014. Spontaneous aggregation of the insulin-derived steric zipper peptide VEALYL results in different aggregation forms with common features. J. Mol. Biol. 426:362–376. [PubMed: 24513105]
123. Soloviev Z, Bullock JMA, James JMB, Sauerwein AC, Nettleship JE, Owens RJ, Hansen DF, Topf M, and Thalassinos K. 2022. Structural mass spectrometry decodes domain interaction and dynamics of the full-length human histone deacetylase 2. Biochim. Biophys. Acta (BBA) - Proteins Proteom. 1870:140759.
124. Allen SJ, Eaton RM, and Bush MF. 2017. Structural dynamics of native-like ions in the gas phase: results from tandem ion mobility of cytochrome *c*. Anal. Chem. 89:7527–7534. [PubMed: 28636328]
125. Eldrid C, Ujma J, Kalfas S, Tomczyk N, Giles K, Morris M, and Thalassinos K. 2019. Gas phase stability of protein ions in a cyclic ion mobility spectrometry traveling wave device. Anal. Chem. 91:7554–7561. [PubMed: 31117399]
126. Dixit SM, Polasky DA, and Ruotolo BT. 2018. Collision induced unfolding of isolated proteins in the gas phase: past, present, and future. Curr. Opin. Chem. Biol. 42:93–100. [PubMed: 29207278]
127. Bernstein SL, Liu D, Wyttenbach T, Bowers MT, Lee JC, Gray HB, and Winkler JR. 2004. α-synuclein: stable compact and extended monomeric structures and pH dependence of dimer formation. J. Am. Soc. Mass Spectrom. 15:1435–1443. [PubMed: 15465356]
128. Valentine SJ, Anderson JG, Ellington AD, and Clemmer DE. 1997. Disulfide-intact and -reduced lysozyme in the gas phase: conformations and pathways of folding and unfolding. J. Phys. Chem. B. 101:3891–3900.
129. Ruotolo BT, Hyung S, Robinson PM, Giles K, Bateman RH, and Robinson CV. 2007. Ion mobility–mass spectrometry reveals long-lived, unfolded intermediates in the dissociation of protein complexes. Angew. Chem. Int. Ed. 46:8001–8004.
130. Erba EB, Ruotolo BT, Barsky D, and Robinson CV. 2010. Ion mobility-mass spectrometry reveals the influence of subunit packing and charge on the dissociation of multiprotein complexes. Anal. Chem. 82:9702–9710. [PubMed: 21053918]

131. Pagel K, Hyung S, Ruotolo BT, and Robinson CV. 2010. Alternate dissociation pathways identified in charge-reduced protein complex ions. Anal. Chem. 82:5363–5372. [PubMed: 20481443]

132. Han L, Hyung S, Mayers JJS, and Ruotolo BT. 2011. Bound anions differentially stabilize multiprotein complexes in the absence of bulk solvent. J. Am. Chem. Soc. 133:11358–11367. [PubMed: 21675748]

133. Hernandez-Alba O, Wagner-Rousset E, Beck A, and Cianférani S. 2018. Native mass spectrometry, ion mobility, and collision-induced unfolding for conformational characterization of IgG4 monoclonal antibodies. Anal. Chem. 90:8865–8872. [PubMed: 29956914]

134. Bernstein SL, Dupuis NF, Lazo ND, Wyttenbach T, Condron MM, Bitan G, Teplow DB, Shea JE, Ruotolo BT, Robinson CV, and Bowers MT. 2009. Amyloid-β 2 protein oligomerization and the importance of tetramers and dodecamers in the aetiology of alzheimer's disease. Nat. Chem. 1:2075–2084.

135. Uetrecht C, Barbu IM, Shoemaker GK, van Duijn E, and Heck AJR. 2011. Interrogating viral capsid assembly with ion mobility–mass spectrometry. Nat. Chem. 3:126–132. [PubMed: 21258385]

136. Eldrid C, Ben-Younis A, Ujma J, Britt H, Cragnolini T, Kalfas S, Cooper-Shepherd D, Tomczyk N, Giles K, Morris M, Akter R, Raleigh D, and Thalassinos K. 2021. Cyclic ion mobility–collision activation experiments elucidate protein behavior in the gas phase. J. Am. Soc. Mass Spectrom. 32:1545–1552. [PubMed: 34006100]

137. Eschweiler JD, Martini RM, and Ruotolo BT. 2017. Chemical probes and engineered constructs reveal a detailed unfolding mechanism for a solvent-free multidomain protein. J. Am. Chem. Soc. 139:534–540. [PubMed: 27959526]

138. Tian Y, Han L, Buckner AC, and Ruotolo BT. 2015. Collision induced unfolding of intact antibodies: rapid characterization of disulfide bonding patterns, glycosylation, and structures. Anal. Chem. 87:11509–11515. [PubMed: 26471104]

139. Biehn SE and Lindert S. 2022. Protein structure prediction with mass spectrometry data. Annu. Rev. Phys. Chem. 73:1–19. [PubMed: 34724394]

140. Papadopoulos G, Svendsen A, Boyarkin OV, and Rizzo TR. 2011. Spectroscopy of mobility-selected biomolecular ions. Faraday Discuss. 150:243–255. [PubMed: 22457952]

141. Oomens J, Sartakov BG, Meijer G, and Von Helden G. 2006. Gas-phase infrared multiple photon dissociation spectroscopy of mass-selected molecular ions. International Journal of Mass Spectrometry. 254:1–19.

142. Polewski L, Springer A, Pagel K, and Schalley CA. 2021. Gas-phase structural analysis of supramolecular assemblies. Acc. Chem. Res. 54:2445–2456. [PubMed: 33900743]

143. Jongcheol S. 2020. Advances in ion mobility spectrometry-mass spectrometry (IMS-MS)-based techniques for elucidating higher-order protein structures. Mass Spectrometry Letters. 11:65–70.

144. Le TN, Poully JC, Lecomte F, Nieuwjaer N, Manil B, Desfrançois C, Chirot F, Lemoine J, Dugourd P, van der Rest G, and Grégoire G. 2013. Gas-phase structure of amyloid-β (12 – 28) peptide investigated by infrared spectroscopy, electron capture dissociation and ion mobility mass spectrometry. J. Am. Soc. Mass Spectrom. 24:1937–1949. [PubMed: 24043520]

145. Leavitt CM, Wolk AB, Fournier JA, Kamrath MZ, Garand E, Van Stipdonk MJ, and Johnson MA. 2012. Isomer-specific IR–IR double resonance spectroscopy of D2-tagged protonated dipeptides prepared in a cryogenic ion trap. J. Phys. Chem. Lett. 3:1099–1105. [PubMed: 26288043]

146. Kamrath MZ, Garand E, Jordan PA, Leavitt CM, Wolk AB, Van Stipdonk MJ, Miller SJ, and Johnson MA. 2011. Vibrational characterization of simple peptides using cryogenic infrared photodissociation of H2-tagged, mass-selected ions. J. Am. Chem. Soc. 133:6440–6448. [PubMed: 21449591]

147. Zenobi R. 2015. Coming of age: gas-phase structural information on biomolecules by FRET. Anal. Chem. 87:7497–7498. [PubMed: 26158691]

148. Stryer L. 1978. Fluorescence energy transfer as a spectroscopic ruler. Annual Review of Biochemistry. 47:819–846.

149. Daly S, Poussigue F, Simon A, MacAleese L, Bertorelle F, Chirot F, Antoine R, and Dugourd P. 2014. Action-FRET: probing the molecular conformation of mass-selected gas-phase peptides

with förster resonance energy transfer detected by acceptor-specific fragmentation. Anal. Chem. 86:8798–8804. [PubMed: 25073016]

150. Kulesza A, Daly S, Choi CM, Simon A, Chirot F, MacAleese L, Antoine R, and Dugourd P. 2016. The structure of chromophore-grafted amyloid-β12–28 dimers in the gas-phase: FRET-experiment guided modelling. Phys. Chem. Chem. Phys. 18:9061–9069. [PubMed: 26972232]
151. Kulesza A, Daly S, MacAleese L, Antoine R, and Dugourd P. 2015. Structural exploration and förster theory modeling for the interpretation of gas-phase FRET measurements: chromophore-grafted amyloid-β peptides. The Journal of Chemical Physics. 143:025101. [PubMed: 26178129]
152. Daly S, MacAleese L, Dugourd P, and Chirot F. 2018. Combining structural probes in the gas phase - ion mobility-resolved action-FRET. J. Am. Soc. Mass Spectrom. 29:133–139. [PubMed: 29038996]
153. Langeland J, Lindkvist TT, Kjær C, and Nielsen SB. 2024. Gas-phase förster resonance energy transfer in mass-selected and trapped ions. Mass Spectrometry Reviews. 43:477–499. [PubMed: 36514825]
154. Ilitchev AI, Giammona MJ, Do TD, Wong AG, Buratto SK, Shea J, Raleigh DP, and Bowers MT. 2016. Human islet amyloid polypeptide N-terminus fragment self-assembly: effect of conserved disulfide bond on aggregation propensity. J. Am. Soc. Mass Spectrom. 27:1010–1018. [PubMed: 26894887]
155. Dupuis NF, Wu C, Shea J, and Bowers MT. 2009. Human islet amyloid polypeptide monomers form ordered β-hairpins: a possible direct amyloidogenic precursor. J. Am. Chem. Soc. 131:18283–18292. [PubMed: 19950949]
156. Gilead S and Gazit E. 2008. The role of the 14–20 domain of the islet amyloid polypeptide in amyloid formation. Exp. Diabetes Res. 2008:1–8.
157. Roberts AN, Leighton B, Todd JA, Cockburn D, N Schofield P, Sutton R, Holt S, Boyd Y, Day AJ, and Foot EA. 1989. Molecular and functional characterization of amylin, a peptide associated with type 2 diabetes mellitus. Proc. Natl. Acad. Sci. 86:9662–9666. [PubMed: 2690069]
158. Cornish J, Gallon KE, Lin CQX, Xiao CL, Mulvey TB, Coy DH, Cooper GJS, and Reid IR. 1998. Dissociation of the effects of amylin on osteoblast proliferation and bone resorption. Am. J. Physiol. Endocrinol. Metab. 274:E827–E833.
159. Ridgway Z, Zhang X, Wong AG, Abedini A, Schmidt AM, and Raleigh DP. 2018. Analysis of the role of the conserved disulfide in amyloid formation by human islet amyloid polypeptide in homogeneous and heterogeneous environments. Biochemistry-us. 57:3065–3074.
160. Buchanan LE, Dunkelberger EB, Tran HQ, Cheng P, Chiu C, Cao P, Raleigh DP, de Pablo JJ, Nowick JS, and Zanni MT. 2013. Mechanism of IAPP amyloid fibril formation involves an intermediate with a transient β-sheet. Proc. Natl. Acad. Sci. 110:19285–19290. [PubMed: 24218609]
161. Tenidis K, Waldner M, Bernhagen J, Fischle W, Bergmann M, Weber M, Merkle M, Voelter W, Brunner H, and Kapurniotu A. 2000. Identification of a penta- and hexapeptide of islet amyloid polypeptide (IAPP) with amyloidogenic and cytotoxic properties. J. Mol. Biol. 295:1055–1071. [PubMed: 10656810]
162. Zanuy D, Ma B, and Nussinov R. 2003. Short peptide amyloid organization: stabilities and conformations of the islet amyloid peptide NFGAIL. Biophys. J. 84:1884–1894. [PubMed: 12609890]
163. Azriel R and Gazit E. 2001. Analysis of the minimal amyloid-forming fragment of the islet amyloid polypeptide. J. Biol. Chem. 276:34156–34161. [PubMed: 11445568]
164. Hoffmann W, Folmert K, Moschner J, Huang X, von Berlepsch H, Koksch B, Bowers MT, von Helden G, and Pagel K. 2018. NFGAIL amyloid oligomers: the onset of beta-sheet formation and the mechanism for fibril formation. J. Am. Chem. Soc. 140:244–249. [PubMed: 29235867]
165. Wang L, Ilitchev AI, Giammona MJ, Li F, Buratto SK, and Bowers MT. 2016. Human islet amyloid polypeptide assembly: the key role of the 8–20 fragment. J. Phys. Chem. B. 120:11905–11911. [PubMed: 27785911]
166. Dupuis NF, Wu C, Shea J, and Bowers MT. 2011. The amyloid formation mechanism in human IAPP: dimers have β-strand monomer–monomer interfaces. J. Am. Chem. Soc. 133:7240–7243. [PubMed: 21517093]

167. Shaykhalishahi H, Mirecka EA, Gauhar A, Grüning CSR, Willbold D, Härd T, Stoldt M, and Hoyer W. 2015. A β-hairpin-binding protein for three different disease-related amyloidogenic proteins. ChemBioChem. 16:411–414. [PubMed: 25557164]
168. Heid LF, Agerschou ED, Orr AA, Kupreichyk T, Schneider W, Wördehoff MM, Schwarten M, Willbold D, Tamamis P, Stoldt M, and Hoyer W. 2023. Sequence-based identification of amyloidogenic β-hairpins reveals a prostatic acid phosphatase fragment promoting semen amyloid formation. Comput. Struct. Biotechnol. J. 23:417–430. [PubMed: 38223341]
169. Young LM, Cao P, Raleigh DP, Ashcroft AE, and Radford SE. 2014. Ion mobility spectrometry–mass spectrometry defines the oligomeric intermediates in amylin amyloid formation and the mode of action of inhibitors. J. Am. Chem. Soc. 136:660–670. [PubMed: 24372466]
170. Frousios KK, Iconomidou VA, Karletidi C, and Hamodrakas SJ. 2009. Amyloidogenic determinants are usually not buried. BMC Struct. Biol. 9:44. [PubMed: 19589171]
171. Serrano AL, Lomont JP, Tu L, Raleigh DP, and Zanni MT. 2017. A free energy barrier caused by the refolding of an oligomeric intermediate controls the lag time of amyloid formation by hIAPP. J. Am. Chem. Soc. 139:16748–16758. [PubMed: 29072444]
172. Cabral da Silva D, Fontes GN, Erthal LCS, and Lima LMTR. 2016. Amyloidogenesis of the amylin analogue pramlintide. Biophys. Chem. 219:1–8. [PubMed: 27665170]
173. Miller MET, Li M, Baghai A, Peetz VH, Zhyvoloup A, and Raleigh DP. 2022. Analysis of sheep and goat IAPP provides insight into IAPP amyloidogenicity and cytotoxicity. Biochemistry-us. 61:2531–2545.
174. Andrews MN and Winter R. 2011. Comparing the structural properties of human and rat islet amyloid polypeptide by MD computer simulations. Biophys. Chem. 156:43–50. [PubMed: 21266296]
175. Chakraborty S, Chatterjee B, and Basu S. 2012. A mechanistic insight into the amyloidogenic structure of hIAPP peptide revealed from sequence analysis and molecular dynamics simulation. Biophys. Chem. 168–169:1–9.
176. Alghrably M, Czaban I, Jaremko Ł, and Jaremko M. 2019. Interaction of amylin species with transition metals and membranes. Journal of Inorganic Biochemistry. 191:69–76. [PubMed: 30468944]
177. Hutton JC. 1989. The insulin secretory granule. Diabetologia. 32:271–281. [PubMed: 2526768]
178. Brender JR, Hartman K, Nanga RPR, Popovych N, de la Salud Bea R, Vivekanandan S, Marsh ENG, and Ramamoorthy A. 2010. Role of zinc in human islet amyloid polypeptide aggregation. J. Am. Chem. Soc. 132:8973–8983. [PubMed: 20536124]
179. Łoboda D and Rowińska-Żyrek M. 2017. Zn(II) - pramlintide: stability, binding sites and unexpected aggregation. J. Inorg. Biochem. 174:150–155. [PubMed: 28672144]
180. Moracci L, Crotti S, Traldi P, Agostini M, Cosma C, and Lapolla A. 2023. Role of mass spectrometry in the study of interactions between amylin and metal ions. Mass Spectrometry Reviews. 42.
181. Sinopoli A, Magrì A, Milardi D, Pappalardo M, Pucci P, Flagiello A, Titman JJ, Nicoletti VG, Caruso G, Pappalardo G, and Grasso G. 2014. The role of copper(ii) in the aggregation of human amylin. Metallomics. 6:1841–1852. [PubMed: 25080969]
182. Nemes P and Vertes A. 2007. Laser ablation electrospray ionization for atmospheric pressure, in vivo, and imaging mass spectrometry. Anal. Chem. 79:8098–8106. [PubMed: 17900146]
183. Kooijman PC, Mathew A, Ellis SR, and Heeren RMA. 2021. Infrared laser desorption and electrospray ionisation of non-covalent protein complexes: generation of intact, multiply charged species. Anal. Sens. 1:44–47.
184. Li H, Ha E, Donaldson RP, Jeremic AM, and Vertes A. 2015. Rapid assessment of human amylin aggregation and its inhibition by copper(II) ions by laser ablation electrospray ionization mass spectrometry with ion mobility separation. Anal. Chem. 87:9829–9837. [PubMed: 26352401]
185. DeToma AS, Salamekh S, Ramamoorthy A, and Lim MH. 2012. Misfolded proteins in alzheimer's disease and type II diabetes. Chem, Soc, Rev,. 41:608–621. [PubMed: 21818468]
186. Tomasello MF, Sinopoli A, and Pappalardo G. 2015. On the environmental factors affecting the structural and cytotoxic properties of IAPP peptides. J. Diabetes Res. 2015:1–15.

187. Nedumpully-Govindan P and Ding F. 2015. Inhibition of IAPP aggregation by insulin depends on the insulin oligomeric state regulated by zinc ion concentration. Sci. Rep. 5:8240. [PubMed: 25649462]

188. Ilitchev AI, Giammona MJ, Schwarze JN, Buratto SK, and Bowers MT. 2018. Zinc-induced conformational transitions in human islet amyloid polypeptide and their role in the inhibition of amyloidosis. J. Phys. Chem. B. 122:9852–9859. [PubMed: 30299960]

189. Mirecka EA, Feuerstein S, Gremer L, Schröder GF, Stoldt M, Willbold D, and Hoyer W. 2016. β-hairpin of islet amyloid polypeptide bound to an aggregation inhibitor. Sci. Rep. 6:33474. [PubMed: 27641459]

190. Liu N, Duan M, and Yang M. 2017. Structural properties of human IAPP dimer in membrane environment studied by all-atom molecular dynamics simulations. Sci. Rep. 7:7915. [PubMed: 28801684]

191. Sarell CJ, Stockley PG, and Radford SE. 2013. Assessing the causes and consequences of co-polymerization in amyloid formation. Prion. 7:359–368. [PubMed: 24025483]

192. Krebs MRH, Morozova-Roche LA, Daniel K, Robinson CV, and Dobson CM. 2004. Observation of sequence specificity in the seeding of protein amyloid fibrils. Protein Sci.: Publ. Protein Soc. 13:1933–1938.

193. Middleton CT, Marek P, Cao P, Chiu C, Singh S, Woys AM, de Pablo JJ, Raleigh DP, and Martin T Zanni. 2012. Two-dimensional infrared spectroscopy reveals the complex behaviour of an amyloid fibril inhibitor. Nat. Chem. 4:355–360. [PubMed: 22522254]

194. Sarell CJ, Woods LA, Su Y, Debelouchina GT, Ashcroft AE, Griffin RG, Stockley PG, and Radford SE. 2013. Expanding the repertoire of amyloid polymorphs by Co-polymerization of related protein precursors. J. Biol. Chem. 288:7327–7337. [PubMed: 23329840]

195. O'Nuallain B, Williams AD, Westermark P, and Wetzel R. 2004. Seeding specificity in amyloid growth induced by heterologous fibrils. J. Biol. Chem. 279:17490–17499. [PubMed: 14752113]

196. Iannuzzi C, Irace G, and Sirangelo I. 2015. The effect of glycosaminoglycans (GAGs) on amyloid aggregation and toxicity. Molecules. 20:2510–2528. [PubMed: 25648594]

197. Sehlin D, Fang XT, Cato L, Antoni G, Lannfelt L, and Syvänen S. 2016. Antibody-based PET imaging of amyloid beta in mouse models of alzheimer's disease. Nat. Commun. 7:10759. [PubMed: 26892305]

198. Young LM, Tu L, Raleigh DP, Ashcroft AE, and Radford SE. 2017. Understanding co-polymerization in amyloid formation by direct observation of mixed oligomers. Chem. Sci. 8:5030–5040. [PubMed: 28970890]

199. Young LM, Saunders JC, Mahood RA, Revill CH, Foster RJ, Tu L, Raleigh DP, Radford SE, and Ashcroft AE. 2015. Screening and classifying small-molecule inhibitors of amyloid formation using ion mobility spectrometry–mass spectrometry. Nat. Chem. 7:73–81. [PubMed: 25515893]

200. Summers DW, Douglas PM, and Cyr DM. 2009. Prion propagation by Hsp40 molecular chaperones. Prion. 3:59–64. [PubMed: 19535913]

201. Norrby E. 2011. Prions and protein-folding diseases. J. Intern. Med. 270:1–14. [PubMed: 21481020]

202. Bradley ME, Edskes HK, Hong JY, Wickner RB, and Liebman SW. 2002. Interactions among prions and prion "strains" in yeast. Proc. Natl. Acad. Sci. 99:16392–16399. [PubMed: 12149514]

203. Nussbaum JM, Schilling S, Cynis H, Silva A, Swanson E, Wangsanut T, Tayler K, Wiltgen B, Hatami A, Rönicke R, Reymann K, Hutter-Paier B, Alexandru A, Jagla W, Graubner S, Glabe CG, Demuth H, and Bloom GS. 2012. Prion-like behaviour and tau-dependent cytotoxicity of pyroglutamylated amyloid-β. Nature. 485:651–655. [PubMed: 22660329]

204. Arya S, Claud SL, Cantrell KL, and Bowers MT. 2019. Catalytic prion-like cross-talk between a key alzheimer's disease tau-fragment r3 and the type 2 diabetes peptide iapp. ACS Chem. Neurosci. 10:4757–4765. [PubMed: 31642657]

205. Leney AC, Pashley CL, Scarff CA, Radford SE, and Ashcroft AE. 2014. Insights into the role of the beta-2 microglobulin D-strand in amyloid propensity revealed by mass spectrometry. Mol, BioSyst,. 10:412–420. [PubMed: 24336936]

206. McDade E and Bateman RJ. 2017. Stop alzheimer's before it starts. Nature. 547:153–155. [PubMed: 28703214]

207. Hernández H and Robinson CV. 2007. Determining the stoichiometry and interactions of macromolecular assemblies from mass spectrometry. Nat. Protoc. 2:715–726. [PubMed: 17406634]

208. Young LM, Saunders JC, Mahood RA, Revill CH, Foster RJ, Ashcroft AE, and Radford SE. 2016. ESI-IMS–MS: a method for rapid analysis of protein aggregation and its inhibition by small molecules. Methods. 95:62–69. [PubMed: 26007606]

209. Tang K, Li F, Shvartsburg AA, Strittmatter EF, and Smith RD. 2005. Two-dimensional gas-phase separations coupled to mass spectrometry for analysis of complex mixtures. Anal. Chem. 77:6381–6388. [PubMed: 16194103]

210. Shvartsburg AA, Li F, Tang K, and Smith RD. 2006. Characterizing the structures and folding of free proteins using 2-D gas-phase separations: observation of multiple unfolded conformers. Anal. Chem. 78:3304–3315. [PubMed: 16689531]

211. Koeniger SL, Merenbloom SI, Valentine SJ, Jarrold MF, Udseth HR, Smith RD, and Clemmer DE. 2006. An IMS-IMS analogue of MS-MS. Anal. Chem. 78:4161–4174. [PubMed: 16771547]

212. Liu FC, Ridgeway ME, Park MA, and Bleiholder C. 2018. Tandem trapped ion mobility spectrometry. Analyst. 143:2249–2258. [PubMed: 29594263]

213. Giles K, Ujma J, Wildgoose J, Pringle S, Richardson K, Langridge D, and Green M. 2019. A cyclic ion mobility-mass spectrometry system. Anal. Chem. 91:8564–8573. [PubMed: 31141659]

214. Harrison JA, Pruška A, Bittner P, Muck A, Cooper-Shepherd DA, and Zenobi R. 2022. Advancing cyclic ion mobility mass spectrometry methods for studying biomolecules: toward the conformational dynamics of mega dalton protein aggregates. Anal. Chem. 94:12435–12443. [PubMed: 36049221]

215. Webb IK, Garimella SVB, Tolmachev AV, Chen T, Zhang X, Norheim RV, Prost SA, LaMarche B, Anderson GA, Ibrahim YM, and Smith RD. 2014. Experimental evaluation and optimization of structures for lossless ion manipulations for ion mobility spectrometry with time-of-flight mass spectrometry. Anal. Chem. 86:9169–9176. [PubMed: 25152066]

216. Deng L, Webb IK, Garimella SVB, Hamid AM, Zheng X, Norheim RV, Prost SA, Anderson GA, Sandoval JA, Baker ES, Ibrahim YM, and Smith RD. 2017. Serpentine ultralong path with extended routing (SUPER) high resolution traveling wave ion mobility-MS using structures for lossless ion manipulations. Anal. Chem. 89:4628–4634. [PubMed: 28332832]

217. Hollerbach AL, Li A, Prabhakaran A, Nagy G, Harrilal CP, Conant CR, Norheim RV, Schimelfenig CE, Anderson GA, Garimella SVB, Smith RD, and Ibrahim YM. 2020. Ultra-high-resolution ion mobility separations over extended path lengths and mobility ranges achieved using a multilevel structures for lossless ion manipulations module. Anal. Chem. 92:7972–7979. [PubMed: 32383592]

218. Wojcik R, Nagy G, Attah IK, Webb IK, Garimella SVB, Weitz KK, Hollerbach A, Monroe ME, Ligare MR, Nielson FF, Norheim RV, Renslow RS, Metz TO, Ibrahim YM, and Smith RD. 2019. SLIM ultrahigh resolution ion mobility spectrometry separations of isotopologues and isotopomers reveal mobility shifts due to mass distribution changes. Anal. Chem. 91:11952–11962. [PubMed: 31450886]

219. Beveridge R, Phillips AS, Denbigh L, Saleem HM, MacPhee CE, and Barran PE. 2015. Relating gas phase to solution conformations: lessons from disordered proteins. Proteomics. 15:2872–2883. [PubMed: 25920945]

220. Han JY, Choi TS, and Kim HI. 2018. Molecular role of Ca2+ and hard divalent metal cations on accelerated fibrillation and interfibrillar aggregation of α-synuclein. Sci. Rep. 8:1895. [PubMed: 29382893]

Highlights:

- hIAPP early toxic oligomers are elusive, transient, and structurally dynamic.
- IM-MS elucidates hIAPP oligomerisation conformational dynamics.
- IM-MS aids in high-throughput hIAPP inhibitor screening.
- Tandem IM is promising in providing higher-resolution hIAPP structures.

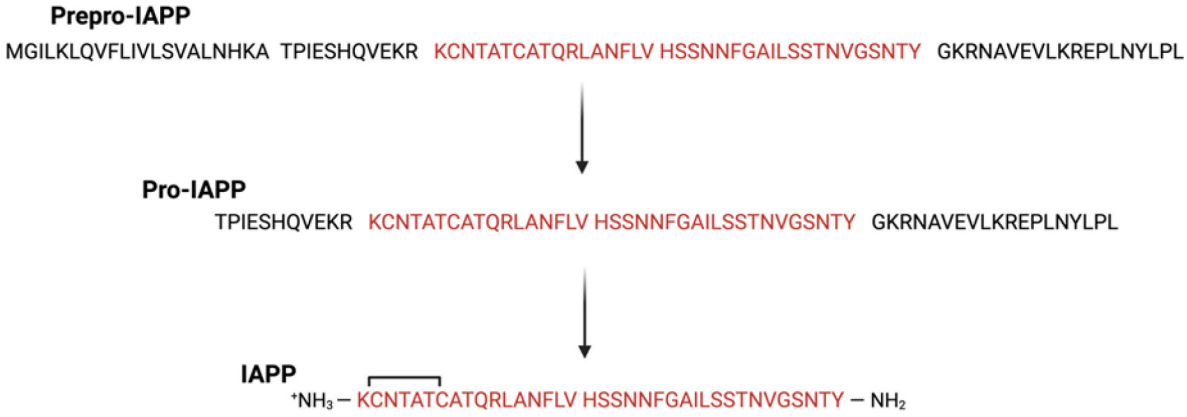

Figure 1.

The sequence of Prepro-IAPP, proIAPP and mature IAPP. The primary sequence of mature IAPP is highlighted in red. The disulphide bond between the Cysteine 2 and Cysteine 7 is also shown in the mature IAPP sequence and the C-terminal amidation is shown. Processing of Pro-IAPP to produce IAPP involves multiple steps and multiple enzymes.

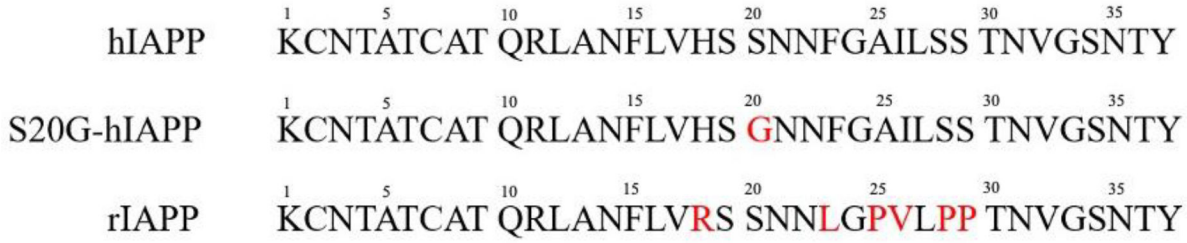

Figure 2.

Sequence of human IAPP (hIAPP), S20G mutant of hIAPP and rat IAPP. Differences in the residues of S20G-hIAPP and rIAPP, relative to the hIAPP sequence, are highlighted in red.

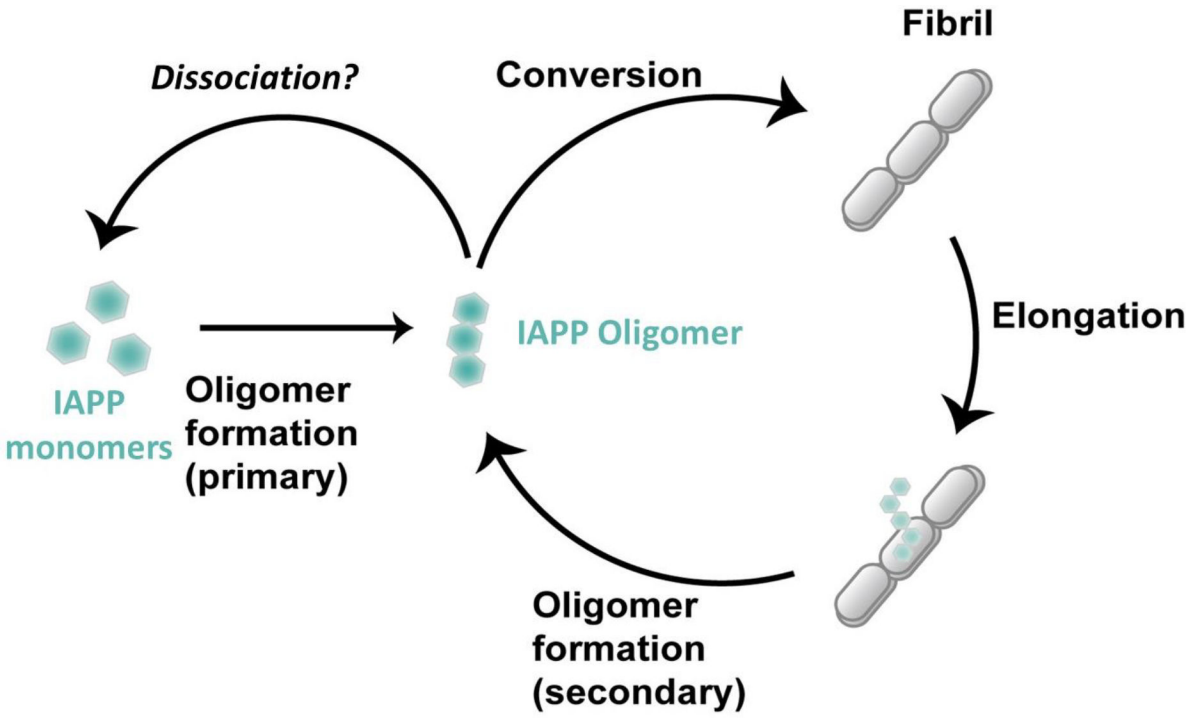

Figure 3.

Schematic illustration of hIAPP amyloid formation. The soluble hIAPP monomers can first assemble into oligomeric intermediates through primary nucleation and elongation. Secondary oligomer formation becomes dominant when a critical amount of fibril is formed, whereby the surface of pre-formed fibrils plays a catalytical role in promoting IAPP oligomer formation. Oligomers can further convert and elongate into fibrils, or the oligomers may potentially dissociate into monomers as reported by Michaels *et al.* using a similar aggregate system. However, experimental data for IAPP oligomers dissociation into monomers by a spontaneous process requires further investigation (67). This figure is patterned after those reported in Camargo et al. and Michaels et al. (70).

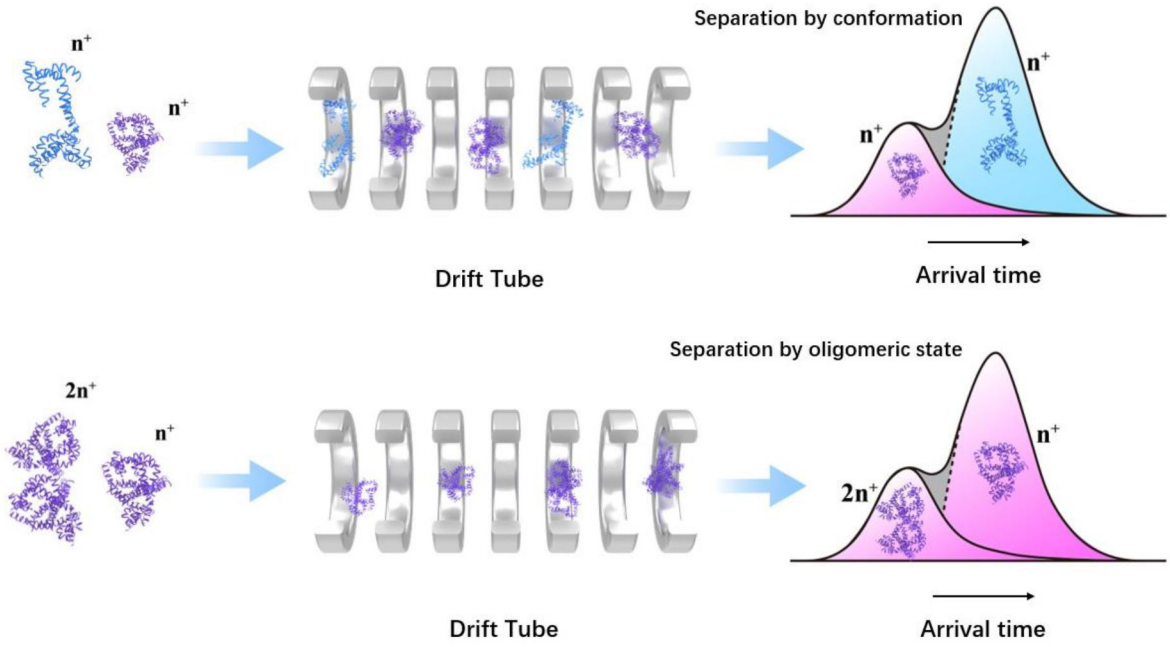

Figure 4.

Schematic illustration of Ion-mobility separation. Top Panel: Ions of the same *m/z* are separated based on their conformation. The ion with a more extended conformation (blue) experiences more collisions with the buffer gas in the drift tube than the compact ion (purple), resulting in a longer arrival time. Bottom Panel: Ions of the same *m/z* are separated based on their oligomeric state. Ions with a higher charge state (annotated as $2n^+$) experience stronger interactions with the electric field, leading to a shorter arrival time compared to ions with a lower charge state (annotated as n^+)

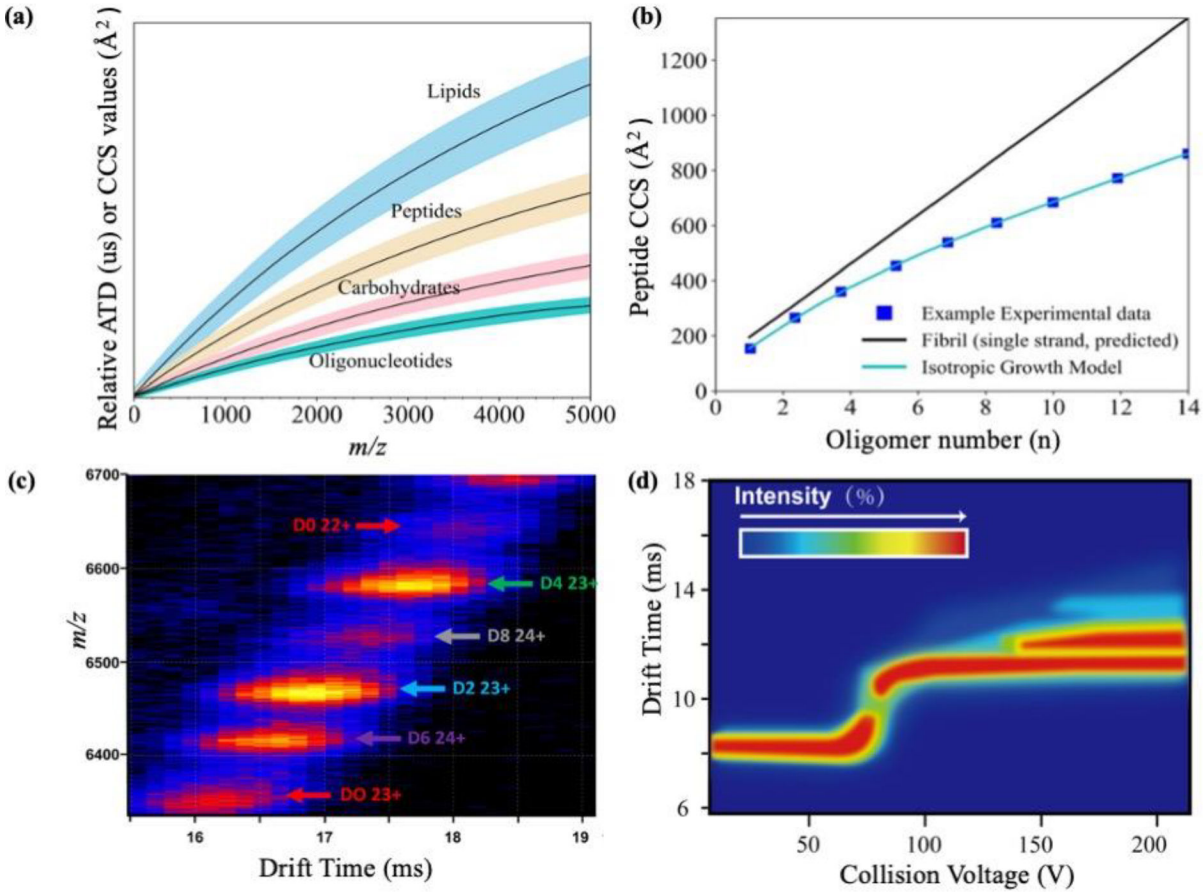

Figure 5.

Representative applications and utility of extracted collision cross-section (CCS) measurements. (a) CCS values are plotted against the mass-to-charge (*m/z*) ratio, delineating the conformational space of diverse biomolecular classes. (b) Correlation of CCS values with oligomeric state (n), with the data fitted to compare against models of fibril growth (depicted by a black solid line) and isotropic growth (shown by a cyan solid line), facilitating the differentiation of oligomer shapes during formation. (c) Driftscope plots from ESI-IM-MS display drift time distributions and relative intensity for the compounds identified. (d) CIU (Collision Induced Unfolding) heatmaps from ESI-IM-MS chart the drift time against an ascending collision voltage (V), typically employed to probe the structural stability of protein ions and their conformational shifts. Figures are re-plotted to demonstrate methods reported in the referenced work (96, 98, 99, 107, 108). Figure 5 (a) is patterned with permission from Anal Bioanal Chem. 2009 May; 394(1): 235–244DOI:10.1007/s00216-009-2666-3. Copyright © 2009, Springer-Verlag. Figure 5 (b) is reprinted with permission from Nat Chem. 2011 February; 3(2): 172–177. doi:10.1038/nchem.945. Copyright © 2010, Springer Nature Limited. Figure 5 (c) is reprinted with permission from Anal. Chem. 2014, 86, 21, 10674–10683. DOI: 10.1021/ac502593n. Copyright © 2014 American Chemical Society. Figure 5 (d) is adapted with permission from Chemical Reviews 2023 123 (6), 2902–2949. DOI: 10.1021/acs.chemrev.2c00600. Copyright © 2023 Emilia Christofi and Perdita Barran.

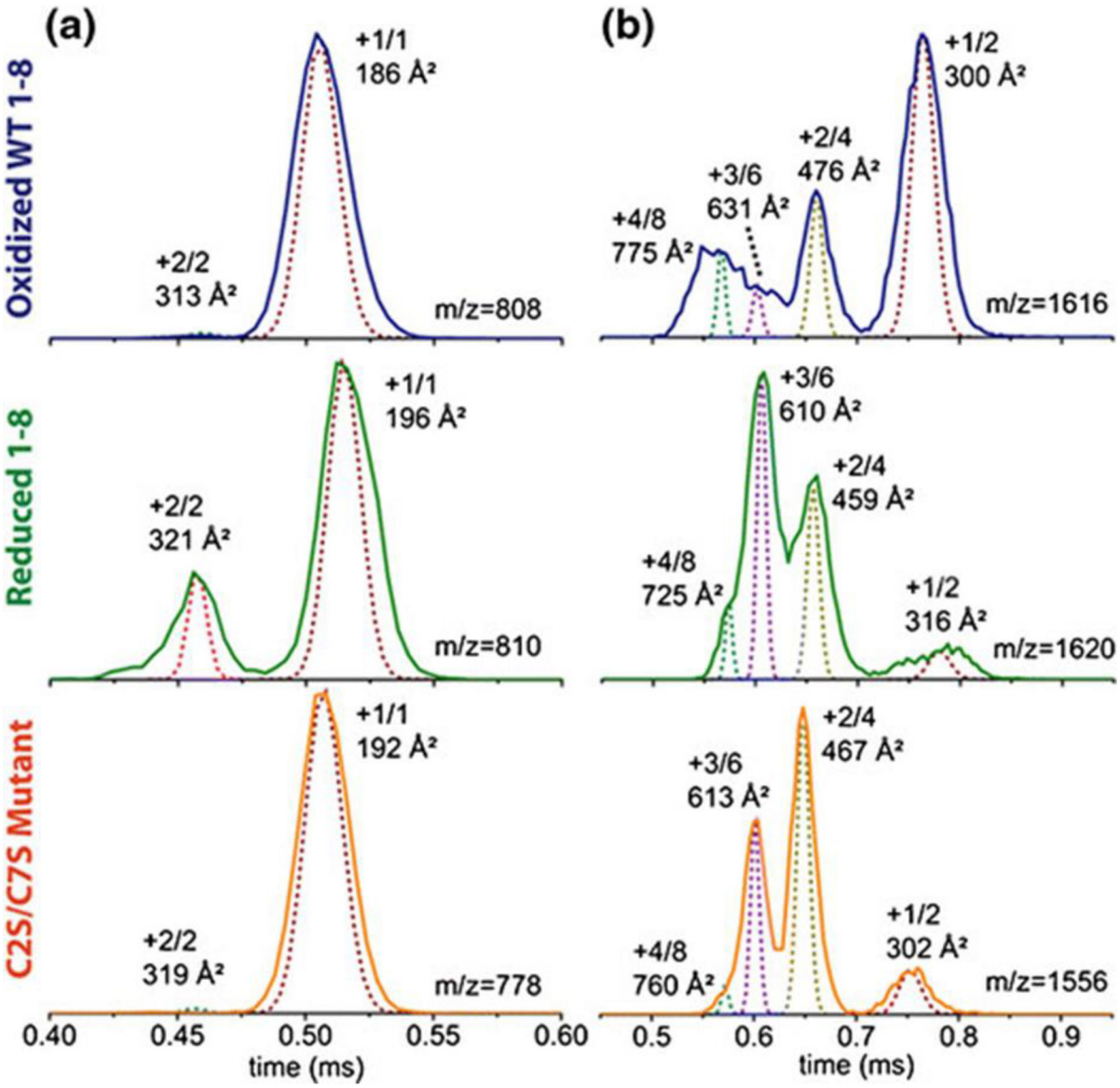

Figure 6.

The ATD of 50 μM hIAPP N-terminal fragment variants at pH 7.4. The WT N-terminal fragment, reduced fragment and the cysteine-to-Serine mutant are represented in blue, green and orange colours, respectively. The peaks are assigned as charge state/oligomer number (z/n). The CCS values for each peak are also shown. J Reprinted with permission from Journal of the American Society for Mass Spectrometry 2016 27 (6), 1010–1018. DOI: 10.1007/s13361-016-1347-7. Copyright 2016 American Chemical Society.

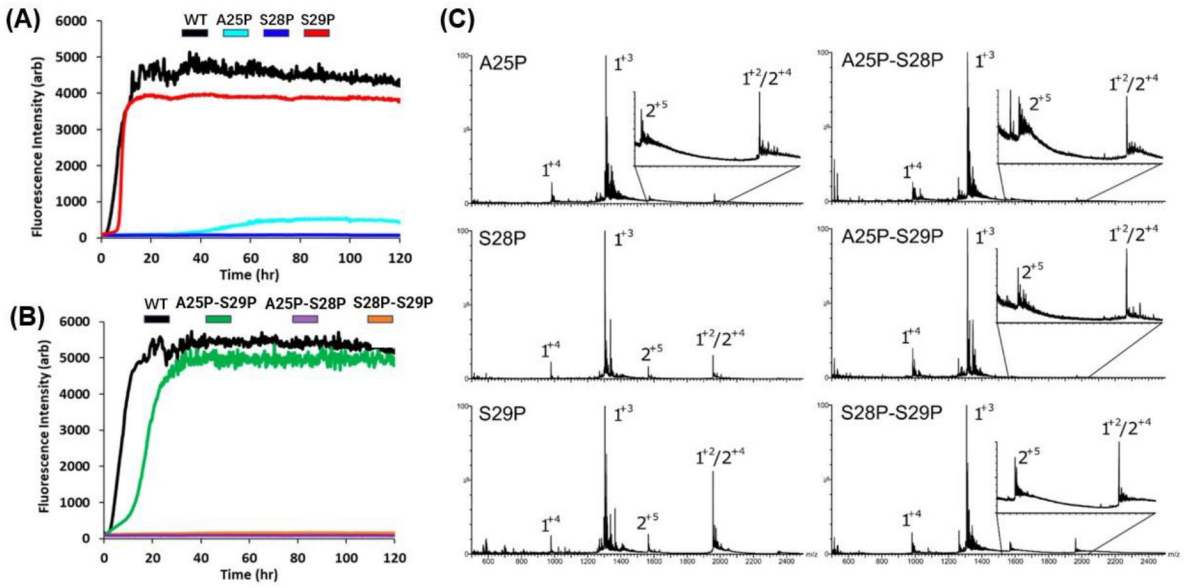

Figure 7.

The effect of proline substitution on the amyloid formation. (A) The temporal aggregation profile of hIAPP and its variants with single proline substitution, as tracked by ThT fluorescence intensity: hIAPP-WT (black), $IAPP_{A25P}$ (cyan), $IAPP_{S28P}$ (blue), and $IAPP_{S29P}$ (red). (B) The temporal aggregation profile of hIAPP and double proline substitution variants, as determined by ThT fluorescence intensity: hIAPP-WT (black), $IAPP_{A25P\ S28P}$(purple), $IAPP_{A25P\ S29P}$ (green) and $IAPP_{S28P\ S29P}$ (orange). (C) ESI-MS spectrum of the hIAPP and proline substitution variants, annotated with their respective oligomeric (n) and ionic (z) states, denoted as $n^{z+\cdot}$ Adapted with permission from ACS Chemical Biology 2020 15 (6), 1408–1416. DOI: 10.1021/acschembio.9b01050. Copyright 2020 American Chemical Society.

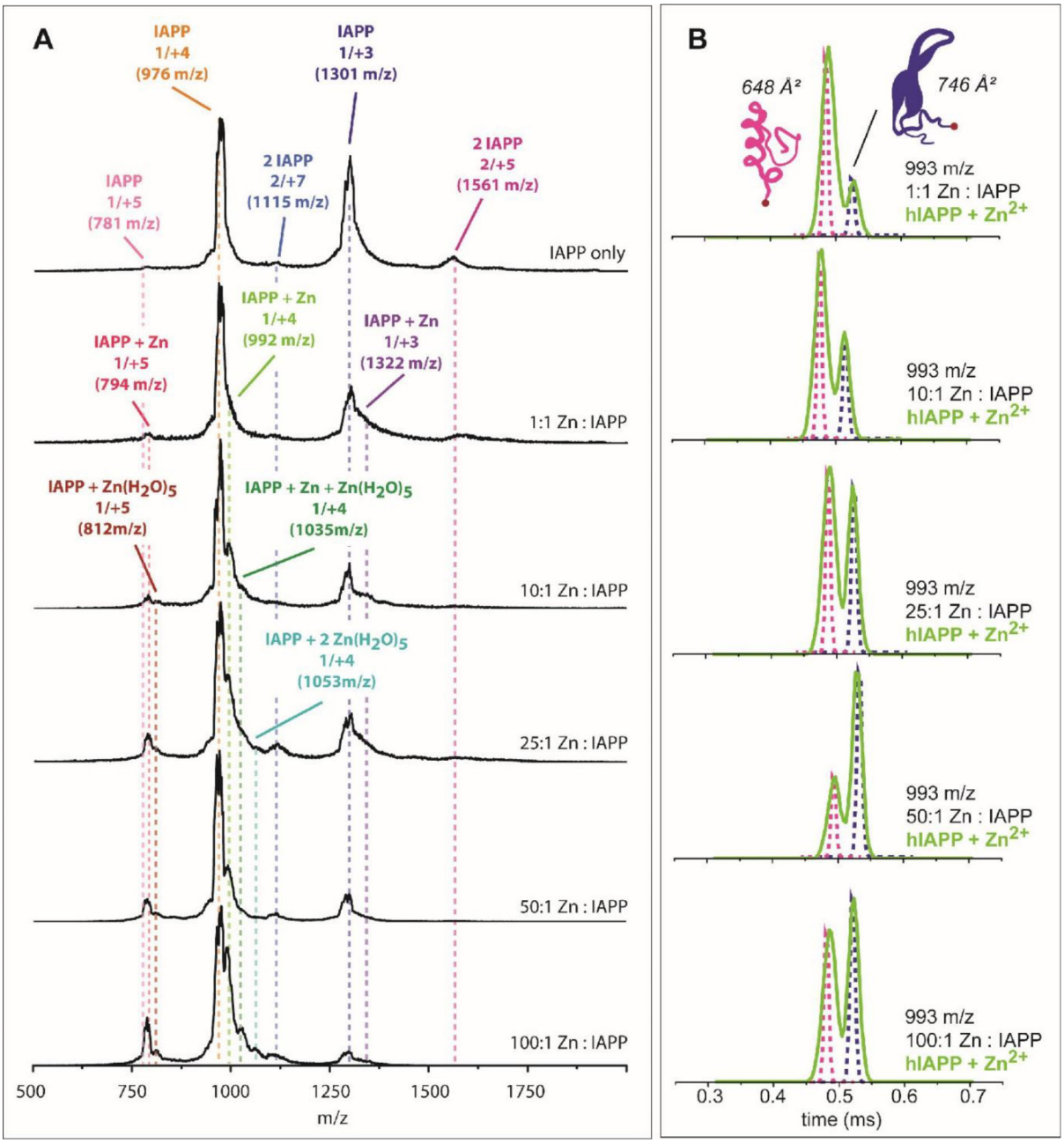

Figure 8.

(A) IM-MS mass spectra of hIAPP under varying zinc concentrations. A shift is observed as the zinc ratio increases. (B) The ATD of the 993 *m/z* peak under varying zinc ratio. Higher zinc concentration increases the abundance of a more extended hIAPP conformation (746 $Å^2$). Reprinted with permission from The Journal of Physical Chemistry B 2018 122 (43), 9852–9859. DOI: 10.1021/acs.jpcb.8b06206. Copyright 2018 American Chemical Society.

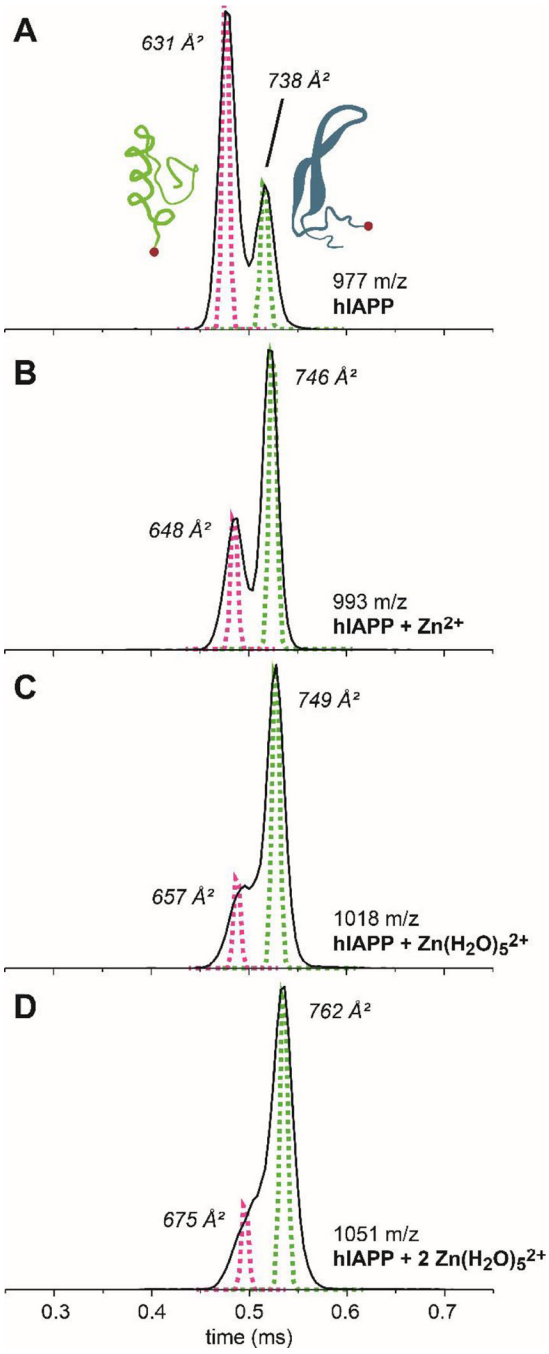

Figure 9.

The ATDs of monomeric 1/+4 hIAPP in the mixture of different types of zinc adducts at a concentration of 50:1 Zn^{2+}/hIAPP. (A) hIAPP alone, (B) hIAPP with anhydrous Zn^{2+}, the peak shift towards an increased abundance of the more extended hIAPP conformation, (C, D) hIAPP with hydrated zinc adducts result in more significant peak shift. Reprinted with permission from The Journal of Physical Chemistry B 2018 122 (43), 9852–9859. DOI: 10.1021/acs.jpcb.8b06206. Copyright 2018 American Chemical Society.

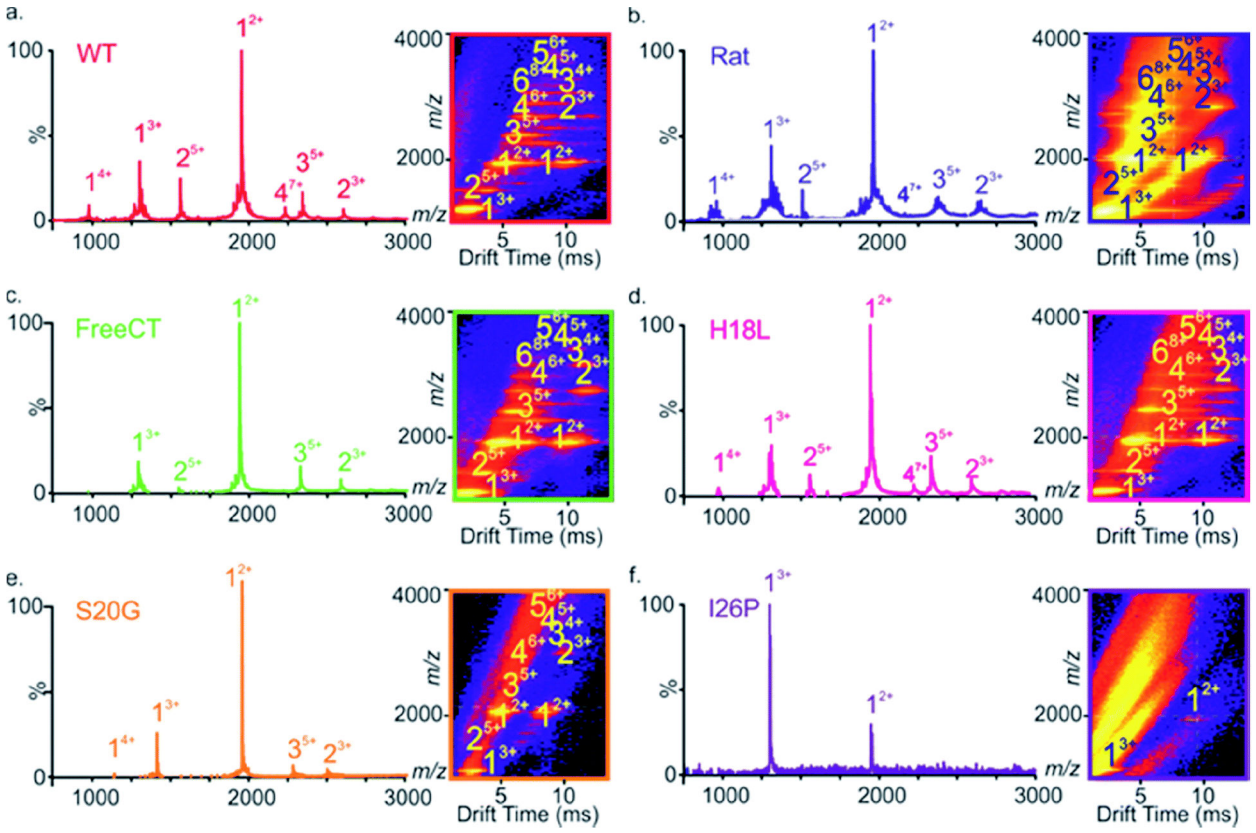

Figure 10.

ESI-mass spectra and ESI-IM-MS Driftscope plots for hIAPP variants. The oligomeric state (n) and charge state (z) are labelled as n^{z+}. The mass spectrum of different IAPP variants exhibits predominantly +2 and +3 monomers and minor amounts of dimers, trimers, and tetramer (except for I26P). The ESI-IM-MS Driftscope plots illustrate the drift time and relative intensity of the oligomers identified. Reprinted with permission from Chemical Science 2017 8,5030. DOI: 10.1039/c7sc00620a. Copyright 2017 Chemical Science.

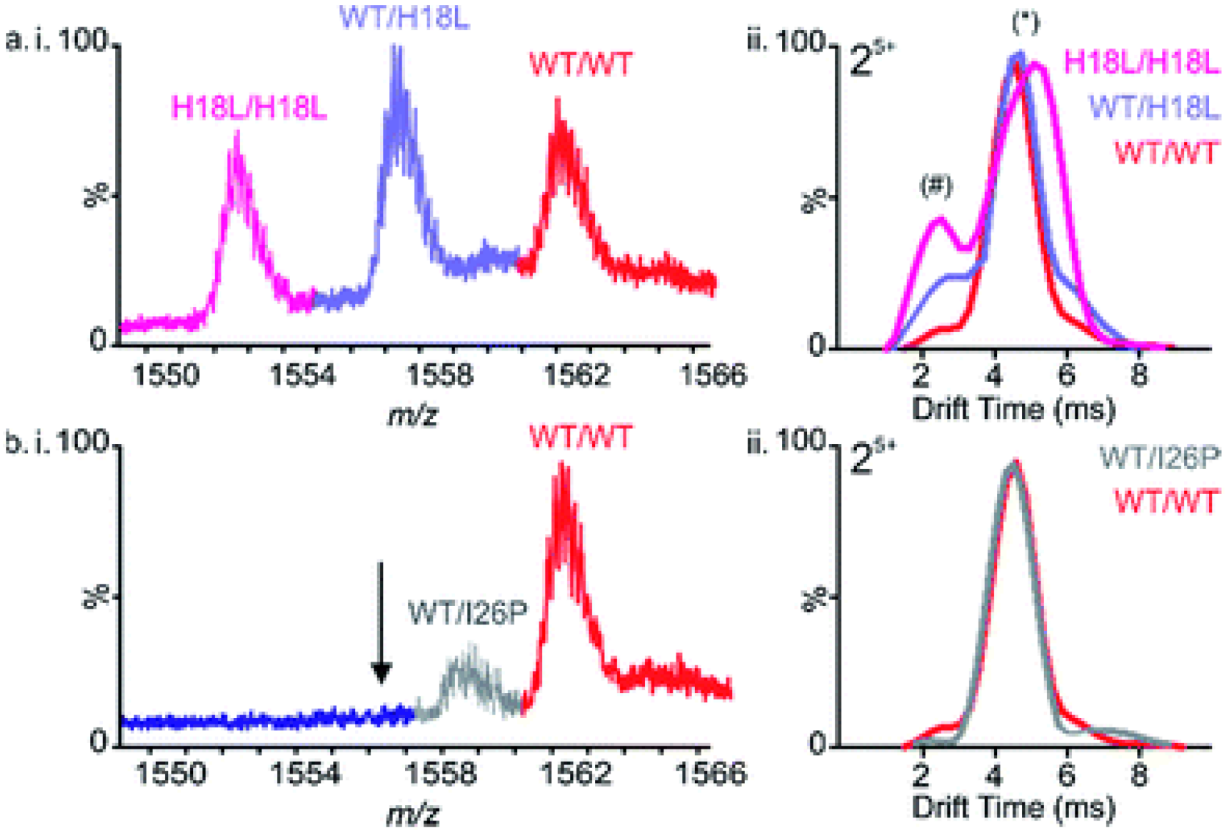

Figure 11.

ESI-mass spectra and arrival time distributions of homo- and hetero-oligomers formed by hIAPP sequence variants. (a) The 1:1 mixture of the wildtype hIAPP and H18L variant, and the +5 charge state homo- and hetero-dimers. (*) indicates a dominant conformation. (#) represents a more compact conformation. (b) The 1:1 mixture of the wild type and I26P. The arrow highlighted the absence of the I26P homodimer. Reprinted with permission from Chemical Science 2017 8,5030. DOI: 10.1039/c7sc00620a. Copyright 2017 Chemical Science.

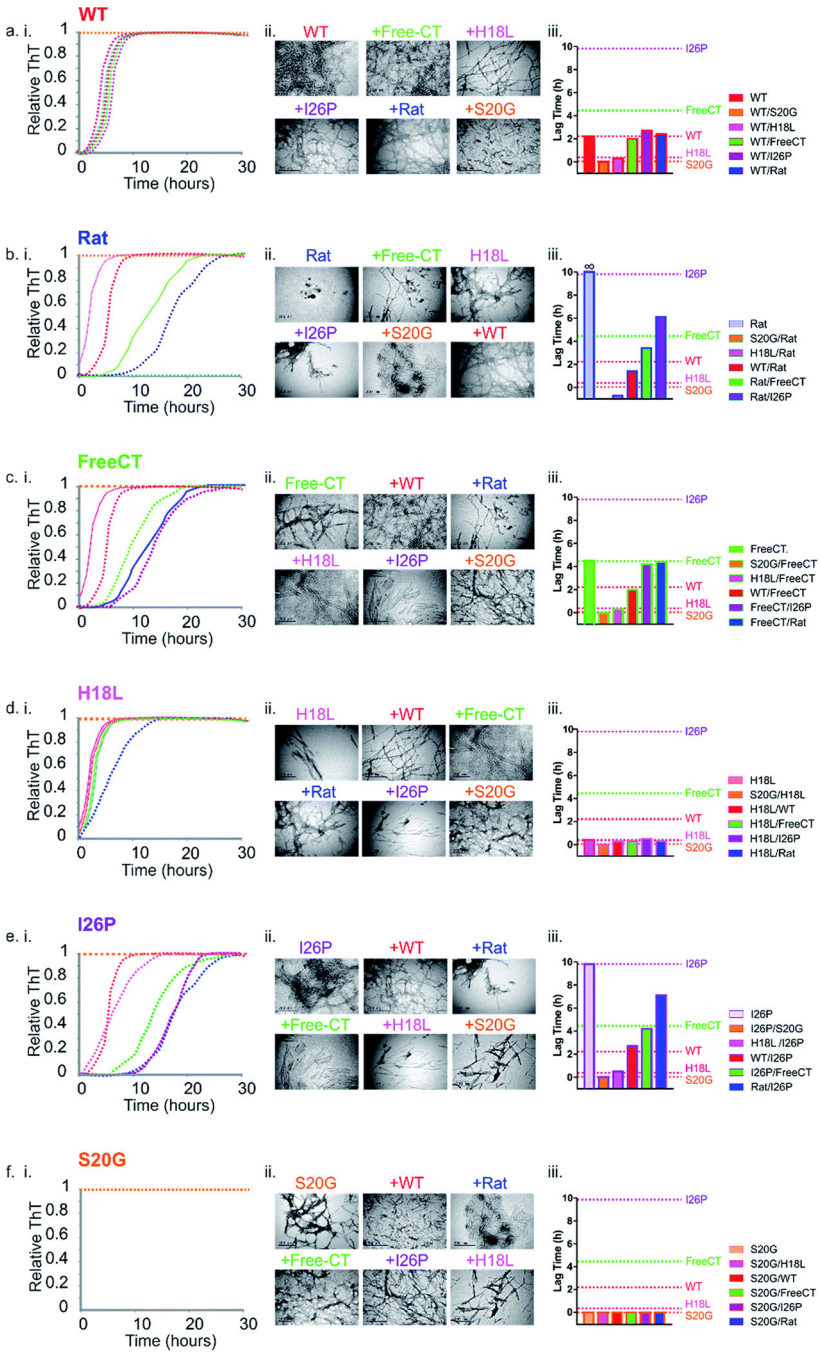

Figure 12.

Fibrillation of the IAPP variants. (a-f) (i) The amyloid formation of hIAPP sequence variants individually and in 1:1 mixture, using ThT fluorescence for tracking, with the variants represented by distinct colours: WT (red), Rat (dark blue), +Free-CT (green), +H18L (red), +I26P (purple), and +S20G (orange). Panel (ii) presents negative stain Transmission Electron Microscopy (TEM) images of each variant's sample after 5 days at 25 °C in a quiescent state. Panels (a-f) (iii) bar chart comparing the lag times derived from ThT fluorescence experiments for 1:1 mixtures of each variant. Reprinted with permission

from Chemical Science 2017 8,5030. DOI: 10.1039/c7sc00620a. Copyright 2017 Chemical Science.

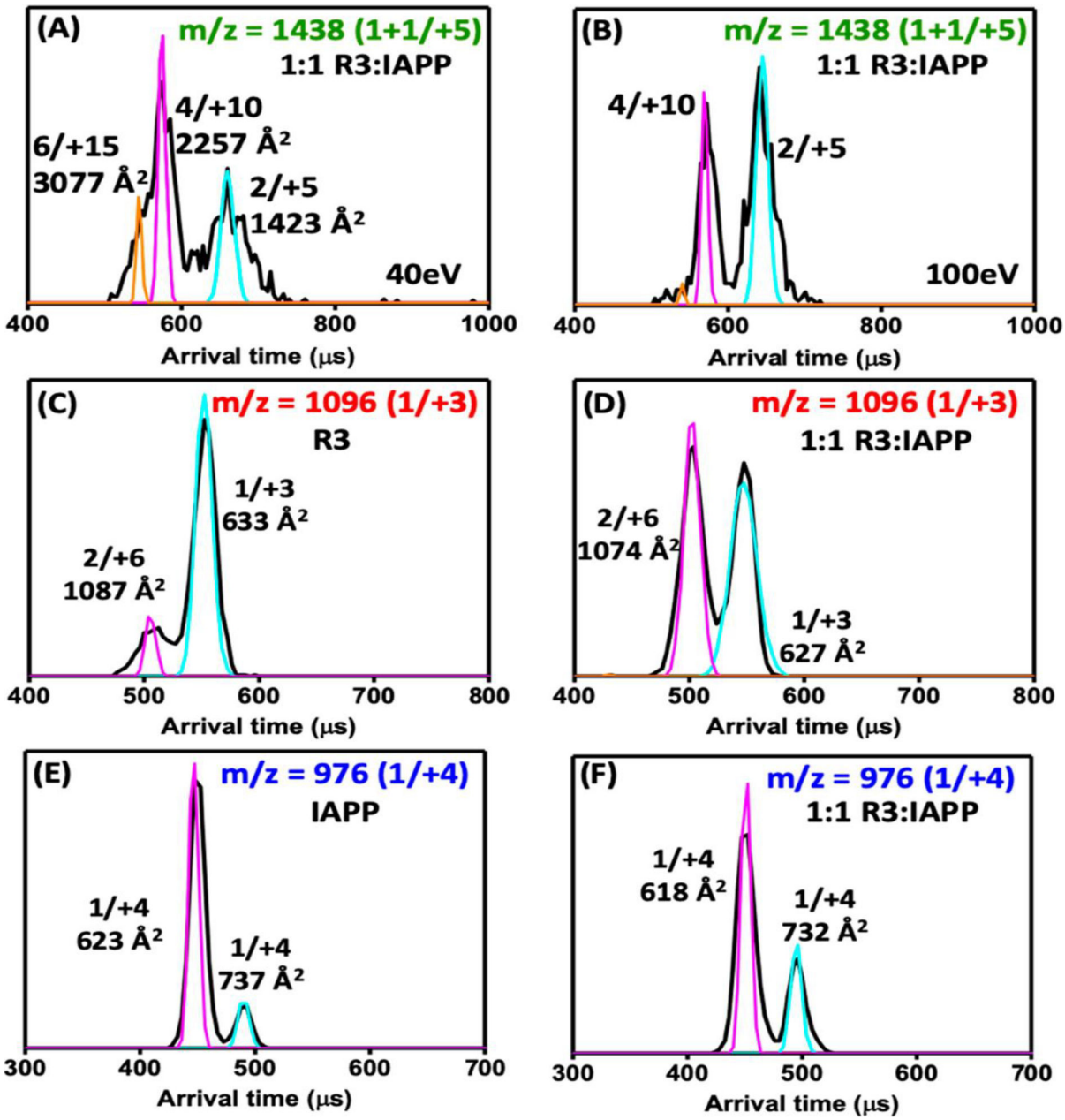

Figure 13.

Arrival Time Distributions (ATDs) depict: (A) and (B) the peak signal for R3-IAPP hetero-oligomers at *m/z* = 1438 under drift cell injection energies of 40 eV and 100eV, respectively; (C) the +3 charge state R3-tau alone; (D) the +3 charge state R3-tau in coexistence with IAPP; (E) the +4 charge state IAPP alone; (F) the +4 charge state IAPP in coexistence with R3-tau. Reprinted with permission from ACS Chemical Neuroscience 2019 10 (11), 4757–4765. DOI: 10.1021/acschemneuro.9b00516. Copyright 2019 American Chemical Society.